A multi-isotope approach towards constraining the origin of large-scale Paleoproterozoic B-(Fe) mineralization in NE China

Aiguo Dong[a], Xiang-kun Zhu[a*], Zhihong Li[a], Brian Kendall[b], Shizhen Li[a], Yue Wang[a], Chao Tang[a]

[a] *MLR Laboratory of Isotope Geology, State Key Laboratory of Continental Dynamics, Institute of Geology, Chinese Academy of Geological Sciences, Beijing 100037, China.*

[b] *Department of Earth and Environmental Sciences, University of Waterloo, 200 University Avenue West, Waterloo, ON, N2L 3G1, Canada*

[*] Corresponding author.

E-mail addresses: xiangkun@cags.ac.cn (X-K Zhu); aiguo.dong@cags.ac.cn (A Dong); bkendall@uwaterloo.ca (B Kendall)

Manuscript accepted for *Precambrian Research*

2017

https://doi.org/10.1016/j.precamres.2017.01.030

ABSTRACT

Borate ore deposits occur predominantly in Phanerozoic evaporative sedimentary environments but are scarce in Precambrian strata. However, massive B- and Mg-rich borate deposits are abundant in the Paleoproterozoic strata of Northeast (NE) China. In addition, several of these borate deposits are dominated by Fe (e.g., >60% Fe_2O_3 content in the Wengquangou deposit). To constrain the origin of these unusual deposits, we obtained B, Fe, and Mg isotope data on the wall rocks and ores of the Mg-rich Houxianyu borate deposit and the Fe-rich Wengquangou borate deposit in NE China. The $\delta^{11}B$ values of the borate deposits (10.66 ± 4.35‰, n = 15) are higher than most types of igneous and

non-evaporative sedimentary rocks, suggesting that B is of evaporative sedimentary origin. However, the borate deposits have a limited range of δ^{56}Fe values near 0‰ (0.05 ± 0.18‰, n = 24), which is similar to igneous rocks and thus points to a magmatic origin for the Fe. The δ^{26}Mg values of the ores and associated rocks (−0.52 ± 0.34‰, n = 24) are intermediate between Mg-rich carbonate rocks and igneous rocks, suggesting a mixed sedimentary and magmatic origin for the Mg. Regional metamorphism and intense deformation modified the deposits significantly by promoting metasomatic alteration of the igneous rocks and evaporite minerals, thus resulting in mixing of magmatic and sedimentary-evaporative sources as well as recrystallization of the sedimentary borate precursors to metamorphic borate minerals. Hence, the B, Fe, and Mg isotope data together with geological and mineralogical observations indicate that formation of the Paleoproterozoic B-(Fe) deposits in NE China involved a three-stage process: enrichment of B and Mg by evaporative sedimentation, introduction of Fe and additional Mg by volcanism, and modification by regional metamorphism/metasomatism.

Key words: B isotopes; Fe isotopes; Mg isotopes; borate deposit; iron deposit; Paleoproterozoic

1 Introduction

Nearly 90% of the world's borate ore deposits occur in younger sedimentary rocks that are associated with evaporative settings, with large amounts of B supplied by hydrothermal or geothermal fluids (Peng and Palmer, 1995; Warren, 2010). Although such deposits are scarce in the Precambrian, a series of Mg-rich and Fe-rich borate deposits

48 occur as a belt (containing more than 25 million metric tons of B_2O_3 and 280 million metric
49 tons of Fe) that is hosted by the Paleoproterozoic strata of Northeast (NE) China (Peng and
50 Palmer, 2002; Liu et al., 2007; Zhang, 1988). Despite the significantly different
51 geochemical properties of B and Fe, some of the borate deposits in the belt co-exist with
52 iron-rich deposits (e.g., the Fe_2O_3 content of magnetite-rich ores is more than 60% in the
53 Wengquangou deposit). In contrast to the Phanerozoic borate deposits (e.g., the Neogene
54 borate deposits in Turkey are dominated by Na-rich and Ca-rich borate minerals, namely
55 ulexite, borax, colemanite, inyoite, and pandermite; Palmer and Helvaci, 1997), these
56 Paleoproterozoic B-(Fe) deposits in NE China have experienced greenschist to amphibolite
57 facies metamorphism and are characterized by Mg-rich and Fe-rich metamorphic borate
58 minerals (e.g., szaibelyite, suanite, ludwigite; Peng and Palmer, 2002; Zhang, 1988).
59 Although many studies have been carried out, the origin of these unusual deposits
60 remains controversial. In general, two major hypotheses have been advanced to explain the
61 origin of the B-(Fe) deposits in NE China: chemical sedimentation (Feng and Zou, 1994;
62 Hu et al., 2015; Jiang et al., 1997; Peng and Palmer, 1995, 2002; Xia et al., 2006; Zhang,
63 1988) and epigenetic-hydrothermal replacement (Liu et al., 2007; Wang and Xu, 1973;
64 Xiao et al., 2003; Yan and Chen, 2014; Zhao and Lin, 2012). For each of these hypotheses,
65 multiple mechanisms have been suggested for borate ore formation. In the scenario of
66 chemical sedimentation, the borate minerals may have precipitated from submarine
67 volcanic exhalative fluids (Feng and Zou, 1994; Zhang, 1988; Xia et al., 2006) or from an
68 evaporating water body (Hu et al., 2015; Jiang et al., 1997; Peng and Palmer, 1995, 2002).
69 In contrast, the epigenetic-hydrothermal replacement hypothesis invokes formation of
70 borate minerals by fluid metasomatism through one of two distinct processes. The borate

71 deposits may represent skarn-type mineralization, with most of the borate minerals and
72 magnetite forming during the later stages of skarnitization (Wang and Xu, 1973; Zhao and
73 Lin, 2012). Alternatively, the borate deposits formed by precipitation from metasomatic
74 fluids that leached the B mainly from B-rich meta-volcanic and sedimentary rocks of the
75 Liaohe Group (Liu et al., 2007; Xiao et al., 2003; Yan and Chen, 2014).

76 Thus, new evidence is needed to resolve the controversy about the origin of these
77 unusual Paleoproterozoic B-(Fe) deposits in NE China and explain the co-existence of Mg-
78 rich and Fe-rich borate deposits. Both types of borate deposit are typically affected by
79 greenschist to amphibolite facies metamorphism. In contrast with traditional stable isotope
80 tracers used to study the borate deposits (e.g., O and S isotopes), the isotopic fractionation
81 of Fe (the major element for mineralization) at the whole-rock scale is limited during
82 regional metamorphism, as inferred from the Fe isotopic characteristics of banded iron
83 formations (BIFs) that experienced greenschist to granulite facies metamorphism in NE
84 China (Li et al., 2008) and Greenland (Dauphas et al., 2004). Furthermore, pronounced Fe
85 isotope fractionations have been observed in BIFs (Dauphas et al., 2004; Frost et al., 2006;
86 Hyslop et al., 2008; Li et al., 2008), metasomatic iron ore deposits (Markl et al., 2006;
87 Wang et al., 2011, 2015), and hydrothermal systems (Rouxel et al., 2008). Redox cycling
88 of Fe exerts a major control on Fe isotope fractionation during chemical sedimentation
89 because of partial oxidation of Fe and because of partial dissimilatory reduction of Fe by
90 microbes (Rouxel et al., 2005; Johnson et al., 2005, 2008). By contrast, very small Fe
91 isotope fractionations are observed during magmatic processes (Chen et al., 2014; Liu et
92 al., 2014; Zhao et al., 2011; Zhu et al., 2013 and references therein), suggesting that Fe
93 isotopes represent a potential proxy for distinguishing between magmatic, sedimentary, and

metasomatic origins for the Fe in borate deposits.

Unlike Fe isotopes, Mg isotopes are not sensitive to redox processes. Pronounced Mg isotopic differences are observed between carbonates and igneous rocks (Saenger and Wang, 2014 and references therein; Teng et al., 2010). Limited Mg isotope fractionation occurs during metamorphic dehydration reactions in a subduction zone setting, as inferred from the similar Mg isotopic compositions of greenschist, amphibolite, and eclogite facies rocks from eastern China (Wang et al., 2014). In addition, endoskarns inherit the Mg isotopic composition of the country dolomitic marbles during contact metamorphism between granodioritic magma and dolomitic marbles (Shen et al., 2013). Hence, these observations suggest that the Mg isotope system also has potential to distinguish between competing hypotheses for the origin of Paleoproterozoic B-(Fe) deposits in NE China, particularly with respect to magmatic versus carbonate sources of Mg.

Marine evaporites and marine carbonates have heavier B isotope compositions than non-marine evaporites and igneous rocks (Frimmel and Jiang, 2001; Jiang et al., 1999; Marschall and Jiang, 2011; Palmer and Helvaci, 1997; Palmer and Slack, 1989; Swihart et al., 1986), suggesting that B isotopes are sensitive tracers for different sources (seawater or crust). During fluid metasomatism, heavier B isotopes are preferentially retained by the fluid whereas lighter B isotopes are incorporated into tourmaline (Palmer et al., 1992). These features suggest that B isotopes can shed insight on the origin of the Paleoproterozoic borate deposits. Previous studies have measured the B isotopic compositions of ore minerals (e.g. szaibelyite, suanite, or ludwigite) and tourmaline in these Paleoproterozoic borate deposits, but despite these efforts, it remains unclear if the B had an evaporative origin or was supplied by metasomatic fluids (Hu et al., 2015; Jiang et

al., 1997; Jiang and Palmer, 1998; Peng and Palmer, 1995, 2002; Xiao et al., 2003; Yan and Chen, 2014). In addition, previous studies mainly focused on the Mg-rich or the Fe-rich borate deposits but have not presented a unified genetic model for both types of borate deposit. Hence, it is necessary to revisit the B isotope data to present a unified genetic model for both types of borate deposit.

Here we use for the first time a combination of B, Fe, and Mg isotope data to further constrain the origin of the Paleoproterozoic B-(Fe) deposits in NE China. Using this multi-isotope approach, we show that a complex set of geological criteria is required to explain the formation of these large Mg-rich and Fe-rich borate deposits, thus accounting for the scarcity of such deposits in the Precambrian rock record.

2 Geological setting

The Jiao-Liao-Ji Belt (JLJB, Fig. 1) is one of three major Paleoproterozoic collisional belts in the North China Craton, whose tectonic setting and evolution may be associated with the opening and closing of an intra-continental rift or, alternatively, an arc-continent collision (reviewed by Zhao and Zhai, 2013). In addition, this belt is endowed with a wealth of ore deposit types such as strata-bound magnesite deposits, SEDEX Pb-Zn deposits, and massive borate deposits (Zhang, 1988; Zhao and Zhai, 2013). The Liaohe Group constitutes a major part of the JLJB and formed ca. 2.2–2.0 Ga. Subsequently, the Liaohe Group was metamorphosed during the collision between the Longgan and Nangrim blocks at ca. 1.90 Ga (Zhao and Zhai, 2013 and references therein). Generally, the Liaohe Group has been subdivided into the North Liaohe Group and the South Liaohe Group based on rock associations and P-T-t paths (Zhao and Zhai, 2013). In ascending stratigraphic order, the

South Liaohe Group comprises the Lieryu Formation, Gaojiyu Formation, Dashiqiao Formation, and Gaixian Formation (Peng and Palmer, 2002; Zhang, 1988; Zhao and Zhai, 2013).

The Lieryu Formation is dominated by fine-grained gneiss and hosts the nearly eighty borate deposits (Fig. 1) that supply 90% of China's industrial B requirements (Liu et al., 2007; Zhang, 1988). These borate deposits are distributed parallel to the fine-grained gneiss and exhibit bedding (Fig. 2). The fine-grained gneiss is mainly composed of quartz, albite, and microcline, and has been interpreted as metamorphosed felsic volcanic rocks (Peng and Palmer, 2002; Zhang, 1988). The fine-grained gneiss contains a minor fraction of dark mafic minerals (e.g., 10% of biotite or amphibole) as well as tourmaline. The borate ores are associated with Mg-rich wall rocks (such as serpentinized rocks and Mg-rich marbles) and are generally subdivided into Mg-rich borate (represented in this study by the Houxianyu deposit) and Fe-rich borate (including iron ore deposits, represented in this study by the Wengquangou deposit) types (Liu et al., 2007; Peng and Palmer, 2002; Zhang, 1988). Tourmalinite is abundant in the Houxianyu deposit, but is less common in the Wengquangou deposit. Generally, it occurs as stratiform layers in the hanging walls of the borate ore bodies, and is composed of tourmaline (>90%) and minor amounts of quartz and feldspar. Additionally, some serpentinized Mg-rich rocks (e.g., peridotites in the Houxianyu deposit) have been interpreted as upper mantle rocks (Hu et al., 2015; Liu et al., 2007) or were formed by the carbonate serpentinization (Zhang, 1988). A further understanding about the petrogenesis of these serpentinized Mg-rich rocks may provide important insights on mantle processes and the geodynamic setting of the JLJB (e.g., Li and Chen, 2014).

The Mg-rich Houxianyu deposit exploited in 1966 is one of the largest borate deposits in the Lieryu Formation (Xia et al., 2006). The orebodies of the Houxianyu deposit have a lenticular morphology (Fig. 2a) and are hosted primarily in serpentinized peridotites (dominated by forsterite and lizardite) and to a lesser extent by serpentinized Mg-rich marbles. The ore bodies and host rocks are crosscut by several diorite and diorite porphyry intrusions (Jiang et al., 1997; Liu et al., 2007). During our field investigation, unaltered Mg-rich marbles were not observed, but some tourmalinite was found in the hanging wall of the ore bodies. Additionally, serpentinization and phlogopitization are widespread in the Houxianyu deposit. The ore minerals include szaibelyite [$Mg_2B_2O_5 \cdot H_2O$], suanite [$Mg_2B_2O_5$] and subordinate ludwigite [$(Fe,Mg)_4Fe_2B_2O_{10}$], which are inferred to be metamorphic minerals. The gangue minerals include forsterite, serpentine, phlogopite, talc, calcite, dolomite, magnesite, tremolite, tourmaline, and minor humite. Szaibelyite generally exhibits a platy, prismatic, or fibrous crystal habit. Fibrous szaibelyite is likely an alteration product of platy metamorphic szaibelyite and suanite during retrograde metamorphism (Jiang et al., 1997). Forsterite in the ores and wall rocks is relatively large and has clear grain boundaries, suggesting recrystallization (Liu et al., 2007; Wang et al., 2006). Sharp grain boundary contacts were observed between forsterite and szaibelyite (Fig. 3f) in the ores and serpentinized peridotites. The alteration minerals serpentine and phlogopite are widespread in the borate ores and host rocks, in some cases comprising more than 50% of some altered peridotites and borate ores. Tourmaline occurs as fine granular clusters, large euhedral crystals, or layers and is mainly found in the orebody as quartz-tourmaline veins and in the hanging wall as tourmalinite (Fig. 3d) or quartz-tourmaline veins (Jiang et al., 1997; Hu et al., 2015). Far from the borate orebody, tourmaline is also

186 preserved in the fine-grained gneisses but has a lower abundance.

187 The Fe-rich Wengquangou deposit contains nearly 280 million tons of iron ore and 21
188 million tons of B_2O_3 (Liu et al., 2007). The orebodies have a shield-shaped morphology
189 and are hosted in Mg-rich marbles and serpentinite (Fig. 2b). Generally, the thickness of
190 the borate-hosting sequence in the Wengquangou deposit (> 800 m) is significantly greater
191 than that in the Houxianyu deposit (Peng and Palmer, 2002). In the Wengquangou deposit,
192 Mg-rich marbles are not common and fresh Mg-rich silicates were not observed during our
193 field investigation. Host rocks represent a significantly lower proportion of the
194 Wengquangou deposit compared with the Houxianyu deposit. A phlogopitization alteration
195 belt with a thickness ranging from 0.2 to several meters is also preserved near the hanging
196 wall (Xia et al., 2006). All geological features indicate intense serpentinization and
197 phlogopitization in the Wengquangou deposit. The ores are generally dominated by B and
198 Fe. Some Fe-rich and B-poor ores could be recognized as iron ores. The ore minerals
199 include ludwigite, magnetite, szaibelyite, and minor suanite. Gangue minerals include
200 lizardite, phlogopite, pyrite, pyrrhotite, forsterite, tourmaline, clinohumite, clinochlore, and
201 calcite. Ludwigite occurs as prismatic, platy, or fibrous forms in the ores, and some
202 ludwigite is suggested to be decomposed to fibrous szaibelyite and fine grained magnetite
203 during retrograde metamorphism (Peng and Palmer, 2002). In hand specimens of the ore,
204 some magnetite is preserved as euhedral or subhedral forms that coexist with the minor
205 amounts of pyrite. Some early-formed magnetite together with forsterite are also preserved
206 as separate bands in association with the borate ores (Peng and Palmer, 2002). Additionally,
207 lizardite and phlogopite are widespread in the ores and host rocks. Fine grained tourmaline
208 is preserved in quartz veins found in both the orebody and wall rocks, with similar features

as the veins observed in the Houxianyu deposit.

3 Materials and methods

3.1 Sample description

A set of ores and wall rocks were collected from the Houxianyu deposit, including six serpentinized peridotites, seven szaibelyite ores, and two tourmalinites. Fresh Mg-rich marbles were not observed in the Houxianyu deposit. Two altered marbles and three serpentinites from the wall rocks as well as seven magnetite ores were obtained from the Wengquangou deposit. In addition, nine magnetite and two pyrite minerals were also separated from the magnetite ores. All samples were collected from outcrop or underground mines that lacked obvious evidence for weathering and phlogopitization. Samples were powdered in an agate mortar for bulk mineralogical and chemical analysis.

3.2 Major elements

Major element concentrations of the wall rock and ore samples were determined by X-ray fluorescence (XRF) spectroscopy at the Australian Laboratory Services Company following measurement of the loss-on-ignition at 1000°C. The analytical precision of major element concentrations is better than 5% based on analysis of standard reference materials. Boron concentrations were determined by inductively coupled plasma atomic emission spectrometry (ICP-AES) after samples were mixed with a sodium peroxide flux and fused in a furnace. The B concentrations were corrected for spectral inter-element interferences and have an analytical precision of better than 10%.

3.3 Boron isotopes

Boron isotope analysis was undertaken at the Salt Lake Analytical and Test Department, Chinese Academy of Sciences. About 0.02 g of whole rock powder was digested by a mixture of 0.05 g Na_2CO_3 and 0.05 g K_2CO_3 at 850°C. A two-stage column procedure involving Amberlite IRA 743 resin and mixed ion exchange resin (Dowex 50WX8 and Ion Exchanger II resin) was used for B purification, following Wang et al. (2002). First, the sample solution was loaded onto conditioned Amberlite IRA 743 resin and eluted with 10 ml of 0.1 M HCl at 75°C. Subsequently, the condensed solution was sequentially passed through a mixed ion exchange resin column, and eluted with 15 ml of ultrapure water. A proper amount of Cs_2CO_3 and mannitol were added into the final eluent for the mass spectrometric analysis.

A Triton thermal ionization mass spectrometer (TIMS, Thermo Fisher Scientific, USA) was used for measuring the isotopic ratio of B. The B isotope data were acquired using a special double cup system for achieving static multi-collection of $Cs_2{}^{10}BO_2{}^+$ (308) and $Cs_2{}^{11}BO_2{}^+$ (309) ions, which were formed by the reaction between the boric acid and Cs_2CO_3. Further description of the analytical method for measurement of B isotopic ratios is provided in Xiao et al. (1988). The B isotopic compositions of the samples are expressed as $\delta^{11}B$ (‰) relative to the NIST SRM 951 standard:

$$\delta^{11}B\ (‰) = [(^{11}B / {}^{10}B)_{sample} / (^{11}B / {}^{10}B)_{SRM951} - 1] \times 1000$$

The measured average $^{11}B/^{10}B$ ratio of NIST SRM 951 is 4.05262 ± 0.00077 (n = 9; 2SD) by using similar column chemistry as samples. The external accuracy based on repeated analyses of a standard solution and a tourmaline standard were less than 1‰. The $\delta^{11}B$ values of one tourmaline laboratory standard (IMR RB2) was −12.10 ± 0.78‰ (n =

5; 2SD), which is consistent with the $\delta^{11}B$ value of −12.53 ± 0.57‰ determined by using the LA-MC-ICP-MS at the Laboratory of Isotope Geology, Institute of Mineral Resources, Chinese Academy of Geological Sciences (CAGS) (Hou et al., 2010), suggesting negligible inter-laboratory biases in B isotope data.

3.4 Iron isotopes

Iron isotope analysis was undertaken at the Laboratory of Isotope Geology, Institute of Geology, CAGS. The Fe isotope analysis followed the methods described by Tang et al. (2006) and Zhu et al. (2002, 2008a). About 0.01 to 0.05 g of whole rock powder (depended on the Fe content) was digested by a mixture of concentrated HNO_3, HCl, and HF in a clean room. Iron was separated using a single-stage column chromatography procedure. The column was filled with AGMP-1 anion exchange resin (100–200 mesh). The sample solution was loaded onto the resin bed in 0.2 ml of 6 M HCl and then washed with 15 ml of 6 M HCl (mixed with 0.001% H_2O_2) progressively to remove ions other than Fe and Zn. Subsequently, Fe was collected by elution in 20 ml of 2 M HCl (mixed with 0.001% H_2O_2). During the column chemistry, at least one basalt standard (BCR-2 or GBW-07105) and one duplicate was processed with each batch of unknown samples.

Iron isotope ratios were determined on a Nu Plasma high resolution multi-collector inductively coupled plasma mass spectrometer (HR-MC-ICP-MS) operating in high-resolution mode and using a standard-sample bracketing (SSB) approach to correct for instrumental mass fractionation. Sample solutions (with Fe concentrations of about 5 μg/ml) were introduced into the mass spectrometer in 0.1 M HNO_3 using a DSN 100 desolvating nebulizer. The difference in Fe concentration between samples and standards was less than

10%. Sample Fe isotopic compositions are reported relative to the reference material IRMM-014 as follows:

$$\delta^{i}Fe\ (‰) = [(^{i}Fe / ^{54}Fe)_{sample} / (^{i}Fe / ^{54}Fe)_{IRMM\text{-}014} - 1] \times 1000;\ i = 56 \text{ or } 57.$$

The long-term external reproducibility of $\delta^{57}Fe$ and $\delta^{56}Fe$, based on repeated analyses of in-house standard solutions, was less than 0.10‰ and 0.08‰ at the 2σ level, respectively (n = 90 in one year; Zhu et al., 2008a). During the course of this study, the $\delta^{56}Fe$ value of the Chinese basaltic reference standard CAGSR-1 (GBW-07105) was determined to be 0.13 ± 0.09‰ (2SD, n = 5), which is statistically indistinguishable from the average of 0.15 ± 0.02‰ (2SD, n = 3) reported by Craddock and Dauphas (2011). The $\delta^{56}Fe$ value of international basaltic standard BCR-2 was determined to be 0.09 ± 0.05‰ (2SD, n = 5), which is also statistically indistinguishable from values reported in previous studies (0.09 ± 0.05‰, Chen et al., 2014; 0.09 ± 0.01‰, Craddock and Dauphas, 2011). Hence, inter-laboratory biases in Fe isotopic compositions are negligible.

3.5 Magnesium isotopes

Magnesium isotope analysis was undertaken at the Laboratory of Isotope Geology, Institute of Geology, CAGS. A two-stage column procedure involving Bio-Rad AG50W-X12 cation resin (200-400 mesh) was used for Mg purification, following Chang et al. (2003) and Li et al. (2008). In the first stage, the sample was loaded, washed, and eluted by 0.3 ml of 2 M HCl, 1 ml of 2 M HCl, and 6 ml of 2 M HCl, respectively. In the second stage, the sample was washed with 12 ml of 0.4 M HCl, followed by collection of Mg in 3 ml of 6 M HCl. During the column chemistry, at least one basaltic standard (BCR-2) and one duplicate were processed with each batch of samples.

Magnesium isotope ratios were measured on a Nu Plasma HR-MC-ICP-MS instrument operating in high-resolution mode and using SSB to correct for instrumental mass fractionation. Samples with Mg concentrations of about 1 μg/ml were introduced into the mass spectrometer in 0.3 M HNO_3 using a DSN 100 desolvating nebulizer. The difference in Mg concentration between samples and standards was less than 10%. Sample Mg isotope compositions are reported relative to the DSM3 standard as follows:

$$\delta^{i}Mg\ (‰) = [(^{i}Mg / ^{24}Mg)_{sample} / (^{i}Mg / ^{24}Mg)_{DSM3} - 1] \times 1000;\ i = 25 \text{ or } 26.$$

The long-term external reproducibility of $\delta^{26}Mg$ and $\delta^{25}Mg$, based on repeated analyses of in-house standard solution CAGSMg2 relative to CAGSMg1, was 0.12‰ and 0.07‰, respectively (2SD, n = 91 in one year; Dong et al., 2016). The average $\delta^{26}Mg$ values of our in-house CAGSMg2 solution and DSM3 (measured against itself) were determined to be −0.37 ± 0.12‰ (2SD, n = 57 in one year) and −0.06 ± 0.08‰ (2SD, n = 10), respectively. During the course of this study, the $\delta^{26}Mg$ value of basalt standard BCR-2 was −0.19 ± 0.05‰ (2SD, n = 3), which is statistically identical to previously published values of −0.16 ± 0.11‰ (Tipper et al., 2008) and hence suggests negligible inter-laboratory biases in Mg isotope data.

4 Results

4.1 Boron isotopes

Boron, iron, and magnesium isotopic compositions of the samples from the Houxianyu and Wengquangou deposits are reported in Table 1. All B isotope data fall into the range of previously published B isotope data for the borate deposits of NE China (Fig. 4). In the Houxianyu deposit, the $\delta^{11}B$ values of the szaibelyite ores cover a limited range from 11.72‰

to 13.49‰ (mean = 12.62 ± 1.27‰, 2SD, n = 6), and are similar to the values for the serpentinized peridotite (mean = 12.36 ± 1.63‰, 2SD, n = 2). The two tourmalinites have $\delta^{11}B$ values of 9.49‰ and 9.89‰ that are intermediate between the crust and modern seawater (Fig. 4). In the Wengquangou deposit, the $\delta^{11}B$ values of the magnetite ores are lower compared with the Houxianyu szaibelyite ores, and cover a limited range from 7.80‰ to 9.52‰ (mean = 8.52 ± 1.38‰, 2SD, n = 6). One sample of serpentinite (wall rock) has a $\delta^{11}B$ value of 8.44‰ that is similar to the values from the magnetite ores.

Based on the B isotope data from the Houxianyu and Wengquangou deposits, three features could be summarized here (Fig. 4). Firstly, all B isotope data of the tourmaline from both deposits (including published data; Hu et al., 2015; Jiang et al., 1997; Jiang and Palmer, 1998; Peng and Palmer, 1995, 2002; Yan and Chen, 2014) show a decreasing trend in $\delta^{11}B$ values from the orebody and wall rocks to the country rocks. Secondly, there is no obvious difference in B isotopic composition between the ores and wall rocks whether in the Houxianyu deposit or in the Wengquangou deposit, but the $\delta^{11}B$ values are obviously different between these two borate deposits. For example, the $\delta^{11}B$ values of borate ores (whole rock) and serpentinized rocks in the Wengquangou deposit are lower (by about 4‰ for the borate ores and about 3‰ for the serpentinized rocks) compared with the Houxianyu deposit. Similarly, the $\delta^{11}B$ values of ludwigite and szaibelyite in the Wengquangou deposit are lower (by about 3‰ for both ludwigite and szaibelyite) compared with the Houxianyu deposit (Jiang et al., 1997; Peng and Palmer, 2002; Hu et al., 2014). Finally, the $\delta^{11}B$ values from the borate minerals, ores (whole rocks), and the wall rocks of both deposits are intermediate between the crust and modern seawater, and are also different from the $\delta^{11}B$ values of marine evaporites and non-marine evaporites (Fig. 4).

347

348 **4.2 Iron isotopes**

349 In the Houxianyu deposit, the $\delta^{56}Fe$ values of the szaibelyite ores and serpentinized
350 peridotite are similar and cover a limited range from −0.11‰ to 0.08‰ (mean = −0.01 ±
351 0.15‰, 2SD, n = 6) and from −0.04‰ to 0.11‰ (mean = 0.04 ± 0.13‰, 2SD, n = 7),
352 respectively (Fig. 5). Similarly, in the Wengquangou deposit, the $\delta^{56}Fe$ values of the bulk
353 magnetite ores cluster around 0.1‰ (mean = 0.07 ± 0.16‰, 2SD, n = 7) and are similar to
354 the $\delta^{56}Fe$ values of the serpentinite wall rocks (mean = 0.10 ± 0.29‰, 2SD, n = 3) (Fig. 5).
355 In brief, the $\delta^{56}Fe$ values from the wall rocks and ores in both borate deposits are close to
356 igneous rock compositions (Craddock and Dauphas, 2011; Zhao et al., 2015). In addition,
357 the magnetite from the ores of the Wengquangou deposit have slightly higher $\delta^{56}Fe$ values
358 (mean = 0.22 ± 0.23‰, 2SD, n = 9). The $\delta^{56}Fe$ values of two pyrites from the ores of the
359 Wengquangou deposit are about −0.01‰ and 0.07‰, which are significantly different from
360 the $\delta^{56}Fe$ of pyrites in modern hydrothermal systems (e.g., −1.90‰ to −0.06‰ for the East
361 Pacific Rise at a latitude of 9-10°N; Rouxel et al., 2008).

362

363 **4.3 Magnesium isotopes**

364 The $\delta^{26}Mg$ values of szaibelyite ores in the Houxianyu deposit cover a narrow range
365 from −0.62‰ to −0.40‰ (mean = −0.50 ± 0.16‰, 2SD, n = 5), except for one sample that
366 has a value of −0.09‰ (HXY12-17) (Fig. 6). Sample HXY12-17 has high K_2O and Al_2O_3
367 contents, implying a potential influence from detrital material. The serpentinized
368 peridotites have $\delta^{26}Mg$ values that are similar to the values for the ores, and range from
369 −0.55‰ to −0.39‰ (mean = −0.48 ± 0.12‰, 2SD, n = 7) (Fig. 6). In the Wengquangou

deposit, the δ^{26}Mg values of the magnetite ores range from −0.91‰ to −0.33‰ (mean = −0.62 ± 0.38‰, 2SD, n = 8), and are similar to the δ^{26}Mg values of the serpentinite wall rocks (−0.80‰ to −0.37‰, mean = −0.53 ± 0.46‰, 2SD, n = 3). In addition, two altered marbles have δ^{26}Mg values of −1.37‰ and −0.81‰. The Mg isotopic compositions of the ores and wall rocks in both borate deposits are generally intermediate between the average for igneous rocks (~ −0.25‰; Teng et al., 2010) and the Mg-rich carbonates of the ca. 2.1 Ga Dashiqiao Formation (~ −1.18‰) (Fig. 6).

5 Discussion

5.1 Boron isotope constraints on the origin of the borate deposits

The serpentinized peridotites, serpentinite rocks, and borate ores (including the iron ores) have high δ^{11}B values (mean = 10.66 ± 4.35‰, 2SD, n = 15), which are consistent with the published δ^{11}B values of the borate minerals (suanite, szaibelyite, and ludwigite; mean = 9.49 ± 5.90‰, 2SD, n = 36) and are higher than continental crust and oceanic basalts (Fig. 4). One source of isotopically heavy B is seawater (reviewed by Marschall and Jiang, 2011), because lighter boron isotopes are preferentially incorporated into sediments and Fe-Mn oxides, leaving behind isotopically heavy boron isotopes in seawater (Vengosh et al., 1992, 1998). In addition, fluids released from dehydration of subducting oceanic lithosphere in subduction zones are also rich in heavy boron isotopes (Marschall and Jiang, 2011; von Hinsberg, 2011). In contrast, isotopically light B is derived from the crust, mantle, and non-marine evaporites (reviewed by Marschall and Jiang, 2011). Metamorphism and fluid metasomatism generally decrease the δ^{11}B values of rocks and ores (Slack et al., 1993). Thus, the high δ^{11}B values of the borate deposits indicate that the

393 B cannot be sourced solely from the surrounding igneous and sedimentary rocks via
394 submarine volcanic exhalative sedimentation or hydrothermal metasomatism. At least one
395 other source of B is required to explain the B isotope data.

396 If fluids from a subducting slab were the major source of B for the borate deposits,
397 then it is possible to produce high $\delta^{11}B$ values in tourmaline similar to the values observed
398 in the tourmalinites (~ 9‰) analyzed in this study. Although the geological setting of the
399 Jiao-Liao-Ji Belt enables this possibility, a subduction fluid origin for the B in the borate
400 deposits is unlikely. The low concentration of B in such fluids does not favor precipitation
401 of highly soluble borate minerals unless the subduction fluid fortuitously had extensive
402 interaction with B-rich evaporites (Jiang et al., 1997). Thus, subducted slab fluids are
403 unlikely to be the major source of B for the borate deposits.

404 One possible explanation to satisfy all B isotope data and the enrichment of B in the
405 borate deposits is that the borate minerals were formed initially via evaporative
406 precipitation. Subsequently, the tourmaline in the wall rocks with high $\delta^{11}B$ values was
407 precipitated by isotopically heavy metamorphic fluids, which leached the B from the
408 precursor sedimentary borate minerals. This explanation for the B isotopes is also
409 consistent with the decreasing trend in $\delta^{11}B$ values in tourmaline from the wall rocks (~
410 8‰) to the country rocks (~ 2‰) (Jiang et al., 1997), which may reflect metasomatic fluid
411 diffusion and mixing with isotopically lighter B derived from surrounding sedimentary and
412 igneous rocks during subsequent metamorphism.

413 It is noted that the $\delta^{11}B$ values of the borate deposits are lower than marine evaporites
414 from Inder (Kazakhstan), Gulf Coast (U.S.A.), Fundy Basin (Canada), and Zechstein Basin
415 (Germany) (Swihart et al., 1986), but higher than non-marine evaporative borate deposits

(e.g., the Neogene borate deposits in western Turkey; Palmer and Helvaci, 1997) (Fig. 4). If evaporating marine seawater is the main source for B enrichment (marine evaporative origin), then precipitation of borate minerals would not occur until the seawater has undergone a high degree of evaporation, because of the highly solubility of borate minerals. Generally, borate minerals are not formed until magnesium sulfate and potash salts are deposited (Palmer and Helvaci, 1997). In this scenario, the marine borate minerals should be associated with vast deposits of halite, Ca sulfate minerals (gypsum/anhydrite), Mg salts, and potash. The best example to illustrate this process is the Inder borate deposits, which are recognized as a typical marine evaporative borate deposit. The borate minerals in the Inder deposits were formed in a salt dome with ~100 m of earlier formed halite and abundant gypsum (Garrett, 1998). However, vast deposits of typical marine evaporite minerals have not been observed in the Paleoproterozoic borate deposits of NE China, indicating that borate was not formed solely by evaporative precipitation of large quantities of Paleoproterozoic seawater.

Given the high $\delta^{11}B$ values of the Paleoproterozoic borate minerals but lack of geological evidence for large-scale precipitation of typical marine evaporite minerals, we suggest that these borate minerals were formed by precipitation from evaporating waters whose B concentration was significantly increased by local hydrothermal fluid inputs, similar to the view of Jiang et al. (1997). The albite-microcline-rich fine-grained gneiss in the borate deposits of NE China may be the equivalents of tuffs and pyroclastic rocks that were altered by Na-K-rich evaporite brines (Peng and Palmer, 2002). Borate mineral precipitation may have occurred in a strongly restricted basin, such that the precipitating fluids have a mixed seawater/hydrothermal-geothermal origin, and thus a chemical

composition that enabled large amounts of borate to precipitate without vast quantities of typical marine evaporite minerals. Although a conclusive marine or non-marine origin cannot be demonstrated from the geology and B isotope geochemistry of these Paleoproterozoic borate deposits, the high $\delta^{11}B$ values indicate that evaporative sedimentation played an important role, and the strata of the borate deposits can be interpreted as metamorphosed evaporites (Jiang et al., 1997; Peng and Palmer, 1995, 2002).

5.2 Iron isotope constraints on the origin of the borate and iron deposits

The $\delta^{56}Fe$ values of rocks and ores in the Paleoproterozoic borate deposits have a limited range and cluster around 0‰ (Table 1 and Fig. 5). The original iron isotopic signatures may have been preserved in the bulk samples despite high-grade metamorphism, a possibility supported by the minimal change in the Fe isotopic compositions of banded iron formations (BIFs) that experienced greenschist to granulite facies metamorphism in NE China (Li et al., 2008) and Greenland (Dauphas et al., 2004). Thus, the narrow range of $\delta^{56}Fe$ values for the rocks and ores from the B-(Fe) deposits were not likely the product of homogenization by amphibolite facies regional metamorphism.

Although previous studies do not provide clear evidence for the source of Fe to the B-(Fe) deposits, three potential sources of Fe have been suggested, namely sedimentary, hydrothermal, and magmatic Fe (Hu et al., 2015; Liu et al., 2007; Peng and Palmer, 1995, 2002; Wang and Xu, 1973; Xia et al., 2006; Zhang, 1988; Zhao and Lin, 2012). Relevant sedimentary processes include oxidation of dissolved Fe^{2+} to Fe^{3+} and precipitation of Fe oxides during evaporative precipitation or submarine volcanic exhalative sedimentation. Pronounced Fe isotope fractionation should accompany Fe redox reactions such that

462 heavier Fe isotopes are preferentially incorporated into Fe oxides during partial oxidation
463 (Balci et al., 2006), following a temperature-dependent Rayleigh fractionation model (Fig.
464 7). According to this model, it is assumed that the precipitated Fe^{3+} phase is in isotopic
465 equilibrium with the aqueous Fe^{2+} phase during its formation but that no further isotopic
466 exchange occurs between the two phases thereafter. Curve I represents the Fe isotopic
467 evolution of the remaining solution, showing the progressive enrichment of the lighter Fe
468 isotopes in the remaining solution as more isotopically heavy Fe^{3+} is precipitated. Curve II
469 represents the Fe isotopic composition of the instantaneous precipitated Fe^{3+} phase in
470 equilibrium with the aqueous Fe^{2+} phase at any one instant, showing that it is possible to
471 precipitate an Fe^{3+} phase with a lighter Fe isotopic composition relative to the initial
472 solution during the later stages of precipitation. Curve III represents the Fe isotopic
473 composition of the accumulative Fe^{3+} phase as a function of its accumulation. The Fe
474 isotopic composition of the accumulative Fe^{3+} phase should be equivalent to the initial
475 solution when all of the Fe in the solution has been precipitated. The Rayleigh fractionation
476 model indicates that partial oxidation of a dissolved Fe^{2+} pool should result in a
477 significantly variable range of $\delta^{56}Fe$ values for the Fe oxides, even producing some
478 negative $\delta^{56}Fe$ values.

479 The best example to illustrate this process in nature is the Precambrian BIFs (e.g.,
480 Dauphas et al., 2004; Hyslop et al., 2008; Li et al., 2008; Fig. 5). The Fe oxides in BIFs are
481 formed by partial oxidation of dissolved Fe^{2+} in the largely anoxic water column (e.g., via
482 anoxygenic photosynthesis or oxygenic photosynthesis in the photic zone), thus
483 preferentially leaving behind the lighter Fe isotopes in seawater (Li et al., 2008; Rouxel et
484 al., 2005). Some BIFs have very light Fe isotope signatures, but such compositions are

485 likely the product of dissimilatory iron reduction by microbes (Hyslop et al., 2008; Johnson
486 et al., 2005, 2008). Variable but generally heavy Fe isotopic compositions are observed in
487 Precambrian BIFs (Fig. 5), with the complementary pool of isotopically light Fe
488 represented by low δ^{56}Fe values in sedimentary pyrites in organic-rich mudrocks (Dauphas
489 et al., 2004; Frost et al., 2006; Hyslop et al., 2008; Li et al., 2008; Johnson et al., 2008;
490 Rouxel et al., 2005; Zhu et al., 2008b). In the Mesoproterozoic, variable but generally high
491 δ^{56}Fe values are also recorded in the sedimentary iron ores of the ca. 1.6 Ga Chuanlinggou
492 Formation of the Changcheng System, North China (Fig. 5; Li and Zhu, 2012), pointing to
493 relatively low dissolved O_2 levels in early Mesoproterozoic seawater (Planavsky et al.,
494 2011).

495 If the Fe in the borate deposits of NE China had a sedimentary origin involving partial
496 oxidation of Fe^{2+} to Fe^{3+}, then the borate ores should have a variable range of Fe isotopic
497 compositions similar to the compositions observed in Precambrian BIFs or sedimentary Fe
498 ores. However, the borate deposits have a limited range of δ^{56}Fe values near 0‰ that are
499 similar to igneous rocks (Fig. 5), thus suggesting that the Fe is not of sedimentary origin.

500 Alternatively, the Fe in these borate deposits may have a hydrothermal origin related
501 to fluid metasomatism. As shown in Fig. 5, hydrothermal Fe ores from Germany and China
502 exhibit a large range of Fe isotopic compositions between –1.5‰ and +0.9‰ (Markl et al.,
503 2006; Wang et al., 2011, 2015). Moreover, the average δ^{56}Fe value of the pyrites in Fe-rich
504 massive sulfides, Fe-Zn-rich chimneys, and Cu-rich chimneys from the East Pacific Rise
505 at a latitude of 9-10°N is −0.27 ± 0.29‰ (2SD, n = 5), −1.03 ± 1.06‰ (2SD, n = 6), and −
506 1.18 ± 0.15‰ (2SD, n = 6) (Rouxel et al., 2008), respectively, suggesting that the pyrite
507 was enriched in lighter Fe isotopes inherited from the hydrothermal fluid (−0.40 ± 0.37‰,

2SD, n = 8). However, Fe isotopes in the borate deposits have a limited range of δ^{56}Fe values between –0.1‰ and +0.4‰, and the two pyrite samples from the magnetite ores of the Wengquangou deposit have δ^{56}Fe values of −0.01‰ and 0.07‰, which is inconsistent with a hydrothermal origin for the Fe in the borate deposits.

Generally, the upper mantle has relatively homogeneous Fe isotopic compositions (δ^{56}Fe = 0.01 ± 0.15‰), similar to or slightly lighter than basalts (δ^{56}Fe = 0.07 ± 0.13‰) (Zhu et al., 2013 and references therein), indicating that igneous rocks have a limited range of Fe isotopic compositions that clusters around 0‰ (Fig. 5). In principle, the Fe isotopic composition of magmatic Fe deposits should be similar to the host igneous rocks (Sun et al., 2013), like that observed for the Panzhihua iron deposits in China (Fig. 5; Wang et al., 2012; Chen et al., 2014). Hence, we conclude from the Fe isotope data that the Fe in the Paleoproterozoic B-(Fe) deposits of NE China is primarily of magmatic origin.

5.3 Magnesium isotope constraints on the origin of the borate deposits

Although there was no conclusive evidence to identify the origin of Mg in the borate deposits, previous studies suggested that the Mg was derived from hydrothermal, sedimentary, or magmatic sources (Hu et al., 2015; Liu et al., 2007; Peng and Palmer, 1995, 2002; Wang and Xu, 1973; Xia et al., 2006; Zhang, 1988; Zhao and Lin, 2012). The δ^{26}Mg values of most ores and associated serpentinized wall rocks in the borate deposits are −0.54 ± 0.41‰ (2SD, n = 14) and −0.49 ± 0.24‰ (2SD, n = 10) (Table 1), respectively, while the δ^{26}Mg values of most globally distributed mid-ocean ridge basalts (MORBs), ocean island basalts (OIBs), and peridotite xenoliths are higher and more homogeneous (ranging from −0.35‰ to −0.18‰, with an average value of −0.25 ± 0.07‰, 2SD, n = 139; Teng et al.,

531 2010) (Fig. 6). Modification of the Mg isotopic compositions during prograde
532 metamorphic dehydration is not likely (Wang et al., 2014). Hence, it is reasonable to
533 speculate that the serpentinized wall rocks are not mantle rocks, as suggested by previous
534 studies (Hu et al., 2015; Wang et al., 2006; Xiao et al., 2003). Here, the δ^{26}Mg of the borate
535 deposits may be explained by two processes: Mg was sourced from a metasomatic
536 hydrothermal fluid, or alternatively, Mg was derived from sedimentary and magmatic
537 sources, and was mixed during later metamorphism. It is noted that these two processes are
538 not mutually exclusive.

539 One possible Mg source to a hydrothermal fluid is leaching of the surrounding Mg-
540 rich carbonates. Dissolution of Mg-rich carbonates should result in the hydrothermal fluid
541 inheriting the Mg isotopic composition of the carbonates if such rocks are the dominant
542 source of Mg to the hydrothermal fluid. An example of this process occurs during
543 skarnitization (interaction between granodioritic magma and dolomitic wall rocks), where
544 Mg is mainly derived from carbonate strata (Shen et al., 2013). The Mg isotopic
545 composition of the Mg-rich endoskarns (−1.69‰ to −2.09‰; Fig 6) is similar to
546 compositions of the dolomitic wall rocks, indicating that the wall rocks were the source of
547 Mg. If the Mg in the borate deposits was originally derived from the Mg-rich carbonate via
548 hydrothermal leaching, then the δ^{26}Mg values of the B-Fe and B-Mg ores should be similar
549 to the surrounding carbonates (δ^{26}Mg: <−1‰). However, the Mg isotopic compositions of
550 the borate deposits (−0.52 ± 0.34‰) are heavier than the Mg-rich marbles of the Dashiqiao
551 Formation (Dong et al., 2016; Fig. 6), suggesting that the Mg was not derived solely from
552 the Mg-rich carbonates via hydrothermal fluids. In addition, assuming a typical
553 hydrothermal fluid chemically interacting on a regional scale with igneous and sedimentary

554 rocks, then the hydrothermal fluid would be rich in Fe. However, as discussed previously,
555 the Fe isotope data do not support the formation of the borate deposits by hydrothermal
556 metasomatism but rather the source of Fe was from magmatic rocks (see section 5.2). Thus,
557 the Mg isotope data from the borate deposits cannot be fully explained by a metasomatic
558 hydrothermal process alone, although we note below that metasomatism likely was a
559 contributing factor.

560 Here, we suggest that the Mg isotopic compositions of the borate deposits reflect
561 mixing of Mg from sedimentary and magmatic endmembers. The first magmatic
562 endmember is magma (mean of ~ −0.25‰). These igneous rocks may be the product of
563 volcanic activity, and covered the initial borate minerals. Subsequently, the volcanic rocks
564 were altered during later metamorphism and metasomatism to form the serpentinized wall
565 rocks. The second sedimentary endmember is suggested to be Mg-rich carbonate (mean of
566 ~ −1.18‰, based on eight analyses of magnesites and Mg-rich marbles from the Dashiqiao
567 Formation of the Liaohe Group, Dong et al., 2016) due to the low Ca and Sr concentrations
568 in the borate deposits (which suggest that dolomite is not the sole Mg source; Fig. 6 and
569 Appendix Table). Abundant Mg-rich carbonate is preserved in the Dashiqiao Formation of
570 the Liaohe Group, suggesting evaporative sedimentation from mixed Mg-rich seawater and
571 hydrothermal/geothermal fluids in a semi-closed basin. The co-existence of Mg-rich
572 marbles and B-rich minerals in the Houxianyu and Wengquangou deposits is consistent
573 with evaporative sedimentation of Mg-rich carbonate together with borate minerals. A
574 possible additional sedimentary endmember may be B-Mg rich minerals (e.g., inderite
575 [$Mg_2B_6O_{11}\cdot 15H_2O$] or pinnoite [$MgB_2O_4\cdot 3H_2O$]) that formed during evaporative
576 sedimentation. If correct, these evaporative borate minerals would be the most important

sedimentary source for Mg during later mineralization. On the other hand, if there was no initial Mg-rich borate mineral precipitation during evaporative sedimentation, then the Mg in these borate deposits was likely derived from just two sources, namely the Mg-rich carbonate rocks and magmatic rocks, with mixing likely promoted by subsequent metasomatic processes.

5.4 Synthesis: A three-stage genetic model for the boron mineralization

As discussed above, the B isotope data indicate that the B originated from evaporative sedimentation of borate minerals. By contrast, the Fe isotope results point to an igneous origin for the Fe. Magnesium isotopic compositions are inconsistent with a single origin for Mg, but instead suggest both evaporative sedimentation and magmatic sources. These apparently conflicting results can be reconciled by a three-stage genetic model, namely: I) B and Mg enrichment via evaporative sedimentation, II) subsequent volcanism covered the evaporative sediments and formed the igneous rocks and magnetite, thus introducing Fe and additional Mg to the deposits, and III) regional metamorphism and deformation resulted in mixing, recrystallization and modification of the deposits, and metasomatic alteration of the Mg and possibly B isotope signatures (Fig. 8).

(I) *Boron and magnesium enrichment via evaporative precipitation*. Intense evaporation occurred in a semi-restricted basin with significant inputs from B-rich hydrothermal/geothermal fluids, resulting in precipitation of Mg-rich carbonates and borate minerals (Fig. 8a). Iron precipitation is insignificant at this stage based on the lack of isotopic evidence for redox-related Fe isotope fractionation. The $\delta^{11}B$ values of the deposits are significantly higher than those of non-marine evaporative borates but yet large

amounts of typical marine evaporite minerals are not associated with the borate deposits. These observations suggest that the precipitating fluids had a chemical composition that enabled large amounts of borate precipitation without significant amounts of halite, Ca sulfate minerals, Mg salts, and potash. In addition, the evaporative sedimentary origin of B is further supported by $\delta^{34}S$ data, which range from 16.1‰ to 23.7‰ in the borate ores and szaibelyite, and from 9.1‰ to 17.3‰ in the pyrite from the borate ores (Hu et al., 2015; Jiang et al., 1997).

(II) *Iron and additional magnesium introduction via volcanic activities*. Volcanic activity occurred after the evaporative sedimentation of Mg- and B-rich borate minerals (Fig. 8b). This magmatic input not only promoted the formation of B-Fe ore bodies, but also provided protective cover for the borate evaporites, which are susceptible to later dissolution. The mechanism of volcanogenic iron ore formation may be similar to the case of Kiruna-type iron ore formation (Nystroem and Henriquez, 1994), the Gushan iron ore deposit in the lower Yangtze river valley of southwest China (Hou et al., 2011; Wang et al., 2014), and some Fe deposits in western China (Hou et al., 2014). In this scenario, magnetite formed during volcanic eruptions, resulting in a spatial association with the silicate rocks. In addition, volcanic-magmatic activity also introduced additional Mg to the borate deposits.

(III) *Metasomatic modification during regional metamorphism*. After evaporative sedimentation and volcanism, the borate deposits experienced greenschist to amphibolite facies regional metamorphism at ca. 1.9 Ga (Zhao and Zhai, 2013; Fig. 8c). Regional metamorphism and the associated strong deformation modified the deposits significantly by: (1) metasomatism of the igneous rocks and sedimentary Mg-rich rocks, causing the

623 $\delta^{26}Mg$ values from the borate deposits to become intermediate in composition between
624 igneous rocks and Mg-rich carbonate rocks of the Dashiqiao Formation; (2) the evaporative
625 borate minerals were recrystallized to metamorphic borate minerals. However, no
626 significant modification of the Fe isotope signature is expected because Fe contents in the
627 original evaporative borate minerals were minimal and the Fe has a predominantly
628 magmatic origin. By contrast, the B and Mg isotopic compositions of the borate minerals
629 were susceptible to metasomatic modification during regional metamorphism, which led
630 to an increase in the $\delta^{26}Mg$ and a possible decrease in the $\delta^{11}B$ of the recrystallized
631 metamorphic borate minerals.

632 The evaporative borate minerals (e.g., inderite [$Mg_2B_6O_{11}\cdot 15H_2O$] or pinnoite
633 [$MgB_2O_4\cdot 3H_2O$]) may have precipitated during evaporative sedimentation, and were
634 transformed to ore minerals (e.g., suanite [$Mg_2B_2O_5$] or szaibelyite [$Mg_2B_2O_5\cdot H_2O$]) with
635 dehydration during regional metamorphism (Peng and Palmer, 1995; Jiang et al., 1997).
636 Moreover, metamorphic reactions involving the igneous rocks, magnesites, and
637 evaporative borates could also generate ore minerals in the borate deposits (e.g., ludwigite
638 [$(Fe,Mg)_4Fe_2B_2O_{10}$], suanite [$Mg_2B_2O_5$], or szaibelyite [$Mg_2B_2O_5\cdot H_2O$]) through the
639 followed chemical reactions (H_3BO_3 could be formed during regional metamorphism via
640 metasomatism of evaporative borates) (Hu et al., 2015 and references therein):

641 $2MgCO_3 + 2H_3BO_3 \rightarrow Mg_2B_2O_5 + 2H_2CO_3 + H_2O$

642 $3MgCO_3 + Fe_3O_4 + 2H_3BO_3 \rightarrow (3MgO\cdot FeO\cdot Fe_2O\cdot B_2O_3) + 3H_2O + 3CO_2$

643 The three-stage model described above is broadly consistent with the model proposed
644 recently by Hu et al. (2015). However, no constraints were provided regarding the origin
645 of Fe and Mg, and the serpentinized peridotites were regard as ultrabasic mantle rocks in

646 that study rather than ultramafic volcanic rocks.

647 The genetic model proposed here is not only compatible with geochemical data
648 obtained in this study and previous studies, but is also consistent with the geological
649 features observed in the borate deposits of NE China. Abundant evaporites were generated
650 at some times during the Precambrian such as the early-middle Paleoproterozoic,
651 suggesting that enough B was available from seawater and hydrothermal/geothermal
652 sources to form the initial evaporative borate deposits. Thus, the key issue for the formation
653 of Precambrian borate deposits is their preservation. Volcanism provides a possible way to
654 protect these evaporites from subsequent alteration because the igneous rocks provide a
655 protective cover on the evaporites. Subsequently, regional metamorphism formed the
656 metamorphic borate minerals (e.g., szaibelyite, suanite, ludwigite), which are more stable.
657 The three-stage model requires a complex set of geological conditions to be achieved for
658 the long-term preservation of borate deposits, thus explaining why borate deposits are
659 scarce in Precambrian strata. Furthermore, the model explains the surprising co-existence
660 of B and Fe enrichment in the borate deposits of NE China.

661

662 **6 Conclusions**

663 (1) The serpentinized wall rocks and borate ores (including the iron ores) have high
664 $\delta^{11}B$ values (mean = 10.66 ± 4.35‰, 2SD, n = 15), which are consistent with the previously
665 published $\delta^{11}B$ values of the borate minerals (suanite, szaibelyite, and ludwigite; mean =
666 9.49 ± 5.90‰, 2SD, n = 36), and are higher than most geological materials. Our preferred
667 explanation for the B isotope data is that the B had an evaporative sedimentary origin.

668 (2) The Fe isotopic compositions of the serpentinized wall rocks and ores are relatively

669 homogeneous and cluster around 0‰, which are different from those expected from redox-
670 related sedimentary processes or hydrothermal metasomatism. Hence, we infer that the Fe
671 in the borate deposits had a magmatic origin.

672 (3) The δ^{26}Mg values of the ores and associated rocks are intermediate between those
673 of Mg-rich carbonate rocks and igneous rocks, indicating that Mg originated from both
674 sedimentary and magmatic sources.

675 (4) Evaporation in a semi-closed water body that was fed by hydrothermal fluids
676 initially formed the evaporative borate minerals and Mg-rich carbonates as the primary
677 starting material. Submarine volcanic-magmatic activity covered the evaporite minerals
678 and introduced Fe and additional Mg to the borate deposits. After the evaporative
679 sedimentation and volcanism, regional metamorphism at ca. 1.9 Ga and associated
680 deformation and metasomatism modified the deposits significantly, leading to mixing and
681 metasomatism between the sedimentary rocks and igneous rocks, and the crystallization of
682 metamorphic borate minerals. Hence, it is concluded that the Paleoproterozoic B-(Fe)
683 deposits in NE China were formed by a three-stage process that included evaporative
684 sedimentation, volcanic-magmatic activity, and regional metamorphism.

685

686 **Acknowledgements**

687 The authors acknowledge Sambuddha Misra for suggestions and comments on the
688 manuscript, Yunqi Ma for B isotope determinations, Suohan Tang and Jin Li for assistance
689 with chemical analyses, Biao Jin, Nick S. Belshaw and Yao Shi for assistance with
690 instrumental analyses, Yong Li, Zhaofu Gao, Chenxu Pan and the engineers from the
691 Houxianyu and Wengquangou borate deposits for field assistance. The paper benefited

692 from the comments and suggestions of Shaoyong Jiang and one anonymous reviewer, and
693 editing from Guochun Zhao and Xianhua Li. This study was financially supported by
694 NSFC (Grant No. 41203004), the MLR Public Benefit Research Foundation of China
695 (Grant No. 201211074), and the State Key Fundamental Program ("973"; Grant No.
696 2012CB416801). B. Kendall acknowledges support from a NSERC Discovery Grant
697 (RGPIN-435930).

698

699 **References**

700 Balci, N., Bullen, T.D., Witte-Lien, K., Shanks, W.C., Motelica, M., Mandernack, K.W., 2006. Iron isotope
701 fractionation during microbially stimulated Fe (II) oxidation and Fe (III) precipitation. Geochimica et
702 Cosmochimica Acta 70, 622-639.
703 Chang, V.T.C., Makishima, A., Belshaw, N.S., O'Nions, R.K., 2003. Purification of Mg from low-Mg
704 biogenic carbonates for isotope ratio determination using multiple collector ICP-MS. J. Anal. At.
705 Spectrom. 18, 296-301.
706 Chen, L.-M., Song, X.-Y., Zhu, X.-K., Zhang, X.-Q., Yu, S.-Y., Yi, J.-N., 2014. Iron isotope fractionation
707 during crystallization and sub-solidus re-equilibration: Constraints from the Baima mafic layered
708 intrusion, SW China. Chemical Geology 380, 97-109.
709 Chaussidon, M., Albarède, F., 1992. Secular boron isotope variations in the continental crust: an ion
710 microprobe study. Earth and Planetary Science Letters 108, 229-241.
711 Chaussidon, M., Jambon, A., 1994. Boron content and isotopic composition of oceanic basalts: geochemical
712 and cosmochemical implications. Earth and Planetary Science Letters 121, 277-291.
713 Craddock, P.R., Dauphas, N., 2011. Iron isotopic compositions of geological reference materials and
714 chondrites. Geostandards and Geoanalytical Research 35, 101-123.
715 Dauphas, N., van Zuilen, M., Wadhwa, M., Davis, A.M., Marty, B., Janney, P.E., 2004. Clues from Fe isotope
716 variations on the origin of early Archean BIFs from Greenland. Science 306, 2077-2080.
717 Dong, A., Zhu, X.-K., Li, S.-Z., Kendall, B., Wang, Y., Gao, Z., 2016. Genesis of a giant Paleoproterozoic
718 strata-bound magnesite deposit: Constraints from Mg isotopes. Precambrian Research 281, 673-683.

719 Feng, B., Zou, R., 1994. Characteristic and gensis of Houxianyu borate deposits in Liaoning, China. Earth
720 Science Frontiers 1, 235-237. (in Chinese)
721 Foster, G., von Strandmann, P.P., Rae, J., 2010. Boron and magnesium isotopic composition of seawater.
722 Geochemistry Geophysics Geosystems 11, Q08015.
723 Frimmel, H.E., Jiang, S.Y., 2001. Marine evaporites from an oceanic island in the Neoproterozoic Adamastor
724 ocean. Precambrian Research 105, 57-71.
725 Frost, C., Von Blanckenburg, F., Schoenberg, R., Frost, B., Swapp, S., 2006. Preservation of Fe isotope
726 heterogeneities during diagenesis and metamorphism of banded iron formation. Contributions to
727 Mineralogy and Petrology 153, 211-235.
728 Garrett, D.E., 1998. Chapter 6 - Marine Borate Occurrences: Isotropic Distribution, Borates. Academic Press,
729 San Diego, pp. 255-303.
730 Hou, K., Li, Y., Xiao, Y., Liu, F., TIian, Y., 2010. In situ boron isotope measurements of natural geological
731 materials by LA-MC-ICP-MS. Chinese Science Bulletin 55, 3305-3311.
732 Hou, T., Zhang, Z., Kusky, T., 2011. Gushan magnetite–apatite deposit in the Ningwu basin, Lower Yangtze
733 River Valley, SE China: Hydrothermal or Kiruna-type? Ore Geology Reviews 43, 333-346.
734 Hu, G., Li, Y., Fan, C., Hou, K., Wang, C., Xie, G., 2014. Marine evaporative genesis of Wengquangou
735 ludwigite deposit in eastern Liaoning Province: Evidences from stable isotopic compositions. Mineral
736 Deposits, 821-832. (in Chinese with English abstract)
737 Hu, G., Li, Y., Fan, C., Hou, K., Zhao, Y., Zeng, L., 2015. In situ LA–MC–ICP–MS boron isotope and zircon
738 U–Pb age determinations of Paleoproterozoic borate deposits in Liaoning Province, northeastern China.
739 Ore Geology Reviews 65, 1127–1141.
740 Hyslop, E.V., Valley, J.W., Johnson, C.M., Beard, B.L., 2008. The effects of metamorphism on O and Fe
741 isotope compositions in the Biwabik Iron Formation, northern Minnesota. Contributions to Mineralogy
742 and Petrology 155, 313-328.
743 Jiang, S.Y., Palmer, M., Peng, Q.M., Yang, J.H., 1997. Chemical and stable isotopic compositions of
744 Proterozoic metamorphosed evaporites and associated tourmalines from the Houxianyu borate deposit,
745 eastern Liaoning, China. Chemical Geology 135, 189-211.
746 Jiang, S.Y., Palmer, M.R., 1998. Boron isotope systematics of Tourmaline from granites and pegmatites: A

747 synthesis. European Journal of Mineralogy 10, 1253-1265.
748 Jiang, S.Y., Palmer, M.R., Slack, J.F., Shaw, D.R., 1999. Boron isotope systematics of tourmaline formation
749 in the Sullivan Pb–Zn–Ag deposit, British Columbia, Canada. Chemical Geology 158, 131-144.
750 Johnson, C.M., Roden, E.E., Welch, S.A., Beard, B.L., 2005. Experimental constraints on Fe isotope
751 fractionation during magnetite and Fe carbonate formation coupled to dissimilatory hydrous ferric oxide
752 reduction. Geochimica et Cosmochimica Acta 69, 963-993.
753 Johnson, C.M., Beard, B.L., Roden, E.E., 2008. The iron isotope fingerprints of redox and biogeochemical
754 cycling in modern and ancient Earth. Annu. Rev. Earth Planet. Sci. 36, 457-493.
755 Li, S.-Z., Zhu, X.-K., He, X., Yang, C., Zhao, X., Tang, S., 2008. Separation of Mg for isotope determination
756 by MC- ICP- MS. Acta Petrological et Mineralogica 27, 449-456. (in Chinese with English abstract)
757 Li, Z., Chen, B., 2014. Geochronology and geochemistry of the Paleoproterozoic meta-basalts from the Jiao-
758 Liao-Ji Belt, North China Craton: Implications for petrogenesis and tectonic setting. Precambrian
759 Research 255, Part 2, 653-667.
760 Li, Z., Zhu, X.-K., Tang, S., 2008. Characters of Fe isotopes and rare earth elements of banded iron formations
761 from Anshan-Benxi area: implications for Fe source. Acta Petrologica et Mineralogica 27, 285-290. (in
762 Chinese with English abstract)
763 Li, Z., Zhu, X.-K., 2012. Geochemical features of Xuanlong type iron ore deposit in Hebei Province and their
764 geological significances 28, 2903-2911.(in Chinese with English abstract)
765 Liu, J., Xiao, R., Wang, W., Wang C., 2007. Regional metallogeny model of borate deposits in Liaodong.
766 Geological Publishing House, Beijing. (in Chinese with English abstract)
767 Liu, P.-P., Zhou, M.-F., Luais, B., Cividini, D., Rollion-Bard, C., 2014. Disequilibrium iron isotopic
768 fractionation during the high-temperature magmatic differentiation of the Baima Fe–Ti oxide-bearing
769 mafic intrusion, SW China. Earth and Planetary Science Letters 399, 21-29.
770 Markl, G., Von Blanckenburg, F., Wagner, T., 2006. Iron isotope fractionation during hydrothermal ore
771 deposition and alteration. Geochimica et Cosmochimica Acta 70, 3011-3030.
772 Marschall, H.R., Jiang, S.Y., 2011. Tourmaline isotopes: No element left behind. Elements 7, 313-319.
773 Nystroem, J.O., Henriquez, F., 1994. Magmatic features of iron ores of the Kiruna type in Chile and Sweden;
774 ore textures and magnetite geochemistry. Economic Geology 89, 820-839.

775 Palmer, M., Helvaci, C., 1997. The boron isotope geochemistry of the Neogene borate deposits of western
776 Turkey. Geochimica et Cosmochimica Acta 61, 3161-3169.
777 Palmer, M., London, D., Morgan, G., Babb, H., 1992. Experimental determination of fractionation of $^{11}B/^{10}B$
778 between tourmaline and aqueous vapor: a temperature-and pressure-dependent isotopic system.
779 Chemical Geology: Isotope Geoscience section 101, 123-129.
780 Palmer, M.R., Slack, J.F., 1989. Boron isotopic composition of tourmaline from massive sulfide deposits and
781 tourmalinites. Contributions to Mineralogy & Petrology 103, 434-451.
782 Peng, Q.-M., Palmer, M., 2002. The Paleoproterozoic Mg and Mg-Fe borate deposits of Liaoning and Jilin
783 Provinces, northeast China. Economic Geology 97, 93-108.
784 Peng, Q.-M., Palmer, M., 1995. The Palaeoproterozoic boron deposits in eastern Liaoning, China: a
785 metamorphosed evaporite. Precambrian Research 72, 185-197.
786 Planavsky, N., McGoldrick, P., Scott, C., Li, C., Reinhard, C., Kelly, A., Chu, X., Bekker, A., Love, G.,
787 Lyons, T., 2011. Widespread iron-rich conditions in the mid-Proterozoic ocean. Nature 477, 448-452.
788 Rouxel, O.J., Bekker, A., Edwards, K.J., 2005. Iron isotope constraints on the Archean and Paleoproterozoic
789 ocean redox state. Science 307, 1088-1091.
790 Rouxel, O.J., Shanks, W.C., Bach, W. and Edwards, K.J., 2008. Integrated Fe-and S-isotope study of seafloor
791 hydrothermal vents at East Pacific Rise 9–10 N. Chemical Geology 252, 214-227.
792 Saenger, C., Wang, Z., 2014. Magnesium isotope fractionation in biogenic and abiogenic carbonates:
793 implications for paleoenvironmental proxies. Quaternary Science Reviews 90, 1-21.
794 Shen, B., Wimpenny, J., Lee, C.-T.A., Yin, Q.-Z., Tollstrup, D., 2013. Magnesium isotope systematics of
795 endoskarns: Implications for wallrock reaction in magma chambers. Chemical Geology 356, 209-215.
796 Slack, J.F., Palmer, M.R., Stevens, B.P., Barnes, R.G., 1993. Origin and significance of tourmaline-rich rocks
797 in the Broken Hill district, Australia. Economic Geology 88, 505-541.
798 Swihart, G.H., Moore, P.B., Callis, E.L., 1986. Boron isotopic composition of marine and nonmarine
799 evaporite borates. Geochimica et Cosmochimica Acta 50, 1297-1301.
800 Sun, J., Zhu, X.-K., Chen, Y., Fang, N., 2013. Iron isotopic constraints on the genesis of Bayan Obo ore
801 deposit, Inner Mongolia, China. Precambrian Research 235, 88-106.
802 Tang, S., Zhu, X.-K., Cai, J., Li, S., He, X., Wang, J., 2006. Cheromatographic separation of Cu, Fe and Zn

using AG MP-1 anion exchange resin for isotope determination by MC-ICPMS. Rock and mineralanalysis 25, 5-8. (in Chinese with English abstract)

Teng, F.-Z., Wadhwa, M., Helz, R.T., 2007. Investigation of magnesium isotope fractionation during basalt differentiation: implications for a chondritic composition of the terrestrial mantle. Earth and Planetary Science Letters 261, 84-92.

Tipper, E.T., Louvat, P., Capmas, F., Galy, A., Gaillardet, J., 2008. Accuracy of stable Mg and Ca isotope data obtained by MC-ICP-MS using the standard addition method. Chemical Geology 257, 65-75.

Vengosh, A., Starinsky, A., Kolodny, Y., Chivas, A.R., Raab, M., 1992. Boron isotope variations during fractional evaporation of sea water: New constraints on the marine vs. nonmarine debate. Geology 20, 799-802.

Vengosh, A., De Lange, G.J., Starinsky, A., 1998. Boron isotope and geochemical evidence for the origin of Urania and Bannock brines at the eastern Mediterranean: effect of water-rock interactions. Geochimica et Cosmochimica Acta 62, 3221-3228.

von Hinsberg, V., 2011. Tourmaline: an ideal indicator of its host. Canadian Mineralogist 49, 1-16.

Wang, Q., Xiao, Y., Wang, Y., Zhang, C., Wei, H., 2002. Boron Separation by the two-step ion-exchange for the isotopic measurement of boron. Chinese Journal of Chemistry 20, 45-50.

Wang, S.-J., Teng, F.-Z., Li, S.-G., Hong, J.-A., 2014. Magnesium isotopic systematics of mafic rocks during continental subduction. Geochimica et Cosmochimica Acta 143, 34-48.

Wang, X., Xu, X., 1973. Formation of Borate deposits in Precambrian of China. Geochemica 1, 12-22. (in Chinese)

Wang, Y., Zhu, X.-K., Mao, J., Li, Z., Cheng, Y., 2011. Iron isotope fractionation during skarn-type metallogeny: A case study of Xinqiao Cu-S-Fe-Au deposit in the Middle-Lower Yangtze valley. Ore Geology Reviews 43, 194-202.

Wang, Y., Zhu X.-K., Mao J., Cheng Y., 2014. Preliminary Fe isotopic study of Gushan ore magma depositin Anhui Province. Mineral Deposits 33, 689-696. (in Chinese with English abstract)

Wang, Y., Zhu, X.-K., Cheng, Y., 2015. Fe isotope behaviors during sulfide-dominated skarn-type mineralisation. Journal of Asian Earth Sciences 103, 374-392.

Wang, S., Zhu, X.-K., Song, X., Chen, L., 2012. Fe Isotopic Characteristics of V-Ti Magnetite Deposit in

Panzhihua Area of Sichuan Province and their genetic implications. Acta Geoscientica Sinica 33, 695-1004. (in Chinese with English abstract)

Warren, J.K., 2010. Evaporites through time: Tectonic, climatic and eustatic controls in marine and nonmarine deposits. Earth-Science Reviews 98, 217-268.

Xia, X., Yan, F., Zhao, Y., Chang, W., 2006. Geological features and ore-forming process of uranium-bearing vonsenite deposit in Liaodong rift , eastern Liaoning Province, China. Mineral Deposits 25, 83-88. (in Chinese with English abstract)

Xiao, R., Takao O., Fei H., Nomura M., 2003. Sedimentary-metamorphic boron deposits and their boron isotopic compositions in eastern Liaoning Province. Geoscience 17, 137-142. (in Chinese with English abstract)

Xiao, Y.K., Beary, E.S., Fassett, J.D., 1988. An improved method for the high-precision isotopic measurement of boron by thermal ionization mass spectrometry. International Journal of Mass Spectrometry & Ion Processes 85, 203-213.

Yan, X.-L., Chen, B., 2014. Chemical and boron isotopic compositions of tourmaline from the Paleoproterozoic Houxianyu borate deposit, NE China: Implications for the origin of borate deposit. Journal of Asian Earth Sciences 94, 252-266.

Zhang, Q., 1988. Early proterozoic tectonic styles and associated mineral deposits of the North China Platform. Precambrian Research 39, 1-29.

Zhao, G., Zhai, M., 2013. Lithotectonic elements of Precambrian basement in the North China Craton: Review and tectonic implications. Gondwana Research 23, 1207-1240.

Zhao, X.-M., Zhang, H.-F., Zhu, X.-K, Tang, S., Yan, B., 2011. Iron isotope evidence for multistage melt-peridotite interactions in the lithospheric mantle of eastern China. Chemical Geology 292-293, 127-139.

Zhao, X.-M., Zhang, H.-F., Zhu, X.-K., Zhu, B., Cao, H.-H., 2015. Effects of melt percolation on iron isotopic variation in peridotites from Yangyuan, North China Craton. Chemical Geology 401, 96-110.

Zhao, Y., Lin, W., 2012. Skarn ore deposit In China. Geological Publishing House, Beijing. (in Chinese with English abstract)

Zhu, X.-K., Guo, Y., Williams, R., O'nions, R., Matthews, A., Belshaw, N., Canters, G., De Waal, E., Weser,

U., Burgess, B., 2002. Mass fractionation processes of transition metal isotopes. Earth and Planetary Science Letters 200, 47-62.

Zhu, X.-K., Li, Z., Zhao, X., Tang, S., He, X., 2008a. High-precision measurements of Fe isotopes using MC-ICP-MS and Fe isotope compositions of geological reference materials. Acta Petrologica et Mineralogica 27, 263-272. (in Chinese with English abstract)

Zhu, X.-K., Li, Z., Tang, S., Li, Y., 2008b. Fe isotope characteristics of early Precambrian pyrite deposits and their geological significance: examples from Shandong and Hebei Provinces. Acta Petrologica et Mineralogica 27, 429-433. (in Chinese with English abstract)

Zhu, X.-K., Wang, Y., Yan, B., Li, J., Dong, A., Li, Z., Sun, J., 2013. Developments of non-traditional stable isotope geochemistry. Bulletin of Mineralogy, Petrology and Geochemistry 32, 651-688. (in Chinese with English abstract)

Figures captions

Figure 1 Sketch geological map and location of the JLJB and borate deposits in NE China. a. Sketch map of the JLJB in the Eastern Block of the NCC, modified from Zhao and Zhai (2013); b. Location and stratigraphy of the borate deposits, modified from Liu et al. (2007); Xia et al. (2006).

Figure 2 Geological maps of the borate deposits in NE China. a. Geological map of the Houxianyu deposit, modified from Liu et al. (2007); b. Geological map of the Wengquangou deposit, modified from Xia et al. (2006).

Figure 3 Photos and photomicrographs of ores and associated rocks from the borate deposits in NE China. a. Serpentinized magnetite ores in the Wengquangou deposit; b. Szaibelyite ores in the Houxianyu deposit; c. Serpentinite in the Wengquangou deposit; d. Tourmalinites in the Houxianyu deposit; e. Photomicrograph of magnetite ores containing magnetite and pyrite (reflected light) f. Photomicrograph of szaibelyite ores containing szaibelyite, olivine, and serpentine (crossed-polarized light); g. Photomicrograph of serpentinized magnetite ores containing magnetite and serpentine (crossed-polarized light); h. Photomicrograph of altered szaibelyite ores containing szaibelyite, serpentine, and olivine. Abbreviations: Mag = magnetite; Srp = serpentine; Ol = olivine; Py = pyrite; Sz = szaibelyite.

Figure 4 Boron isotope compositions of the borate deposits in NE China and comparison with other B reservoirs. Data sources: a from Chaussidon and Albarède (1992); b from Chaussidon and Jambon (1994); c from Foster et al. (2010); d from Palmer

and Helvaci (1997); e and f from Swihart et al. (1986); g from Hu et al. (2015); Jiang et al. (1997); Jiang and Palmer (1998); Peng and Palmer (1995, 2002); Yan and Chen (2014); Xiao et al. (2003).

Figure 5 Iron isotope compositions of BIFs, a hydrothermal ore deposit, a skarn type deposit, a magmatic iron ore deposit, igneous rocks, and the borate deposits in NE China. Data sources: a from Dauphas et al. (2004); b from Li et al. (2008); c from Frost et al. (2006); Hyslop et al. (2008); d from Li and Zhu. (2012); e from Markl et al. (2006); f from Wang et al. (2011); g from Chen et al. (2014); Liu et al. (2014); Wang et al. (2012); h from Zhu et al. (2013) and reference therein.

Figure 6 Magnesium isotope compositions of carbonate rocks, igneous rocks, xenoliths from skarns in the U.S.A., and the borate deposits in NE China. Data sources: a from Shen et al. (2013); b, c and d from Zhu et al., 2013 and reference therein; e from Teng et al. (2010).

Figure 7 Modelling results of Rayleigh fractionation between an aqueous Fe^{2+} phase and a precipitated Fe^{3+} phase at two different temperatures (Fig. 7a at 22°C and Fig. 7b at 70°C). Curve I is for $\delta^{56}Fe$ of the remaining solution. Curve II is for $\delta^{56}Fe$ of an instantaneous precipitated Fe^{3+} phase in equilibrium with the aqueous Fe^{2+} phase. Curve III is for the $\delta^{56}Fe$ of the precipitated Fe^{3+} phase as a function of its accumulation. The dashed line represents the isotope composition of the initial hydrothermal solution ($\delta^{56}Fe$: ~ −0.5‰ from Rouxel et al. (2008)). The value of the fractionation factor α between the

aqueous Fe^{2+} phase and precipitated Fe^{3+} phase is about 1.0029 at 22°C and 1.0020 at 70°C (from Balci et al. (2006) and references therein).

Figure 8 Genetic model for the borate deposits in NE China, modified from Peng and Palmer (2002), Zhang (1998), and Hu et al. (2015).

Table caption

Table 1 Boron, iron, and magnesium isotopic compositions of ores (associated minerals) and rocks from the Paleoproterozoic borate deposits in NE China

Appendix Table Major element concentrations of ores (associated minerals) and rocks from the Paleoproterozoic borate deposits in NE China (units of %)

Figure 1

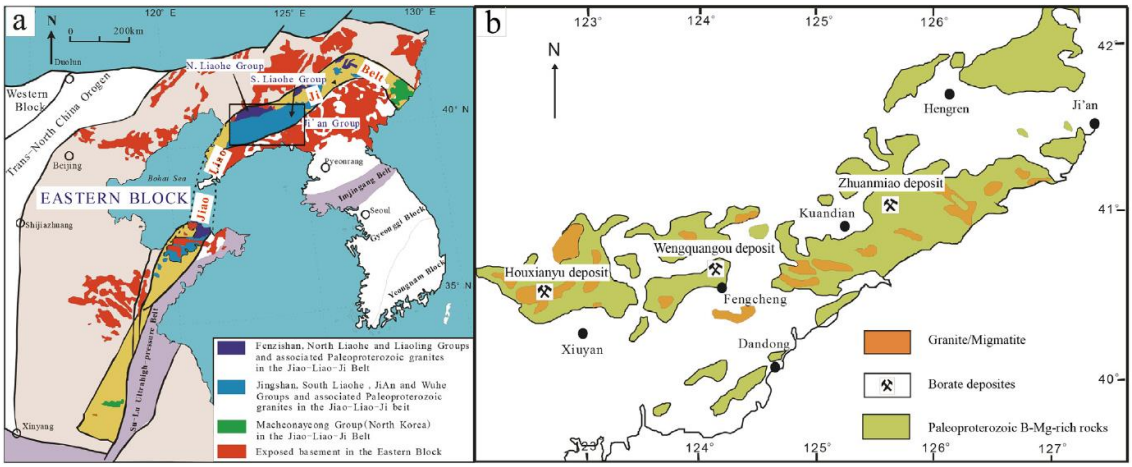
a
N
0
200km
Duolun
Western Block
Trans-North China Orogen
Beijing
Bohai Sea
EASTERN BLOCK
Jiao
Liao
Ji
N. Liaohe Group
S. Liaohe Group
Ji'an Group
Belt
Pyeongnang
Imjingang Belt
Seoul
Gyeonggi Block
Yeongnam Block
Shijiazhuang
Xinyang
Sa-Ta Ultrahigh pressure belt
40° N
35° N
120° E
125° E
130° E
Fenzishan, North Liaohe and Liaoling Groups and associated Paleoproterozoic granites in the Jiao-Liao-Ji Belt
Jingshan, South Liaohe , JiAn and Wuhe Groups and associated Paleoproterozoic granites in the Jiao-Liao-Ji belt
Macheonayeong Group(North Korea) in the Jiao-Liao-Ji Belt
Exposed basement in the Eastern Block
b
N
123°
124°
125°
126°
127°
42°
41°
40°
Hengren
Ji'an
Zhuanmiao deposit
Kuandian
Wengquangou deposit
Houxianyu deposit
Fengcheng
Xiuyan
Dandong
Granite/Migmatite
Borate deposites
Paleoproterozoic B-Mg-rich rocks

Figure 2

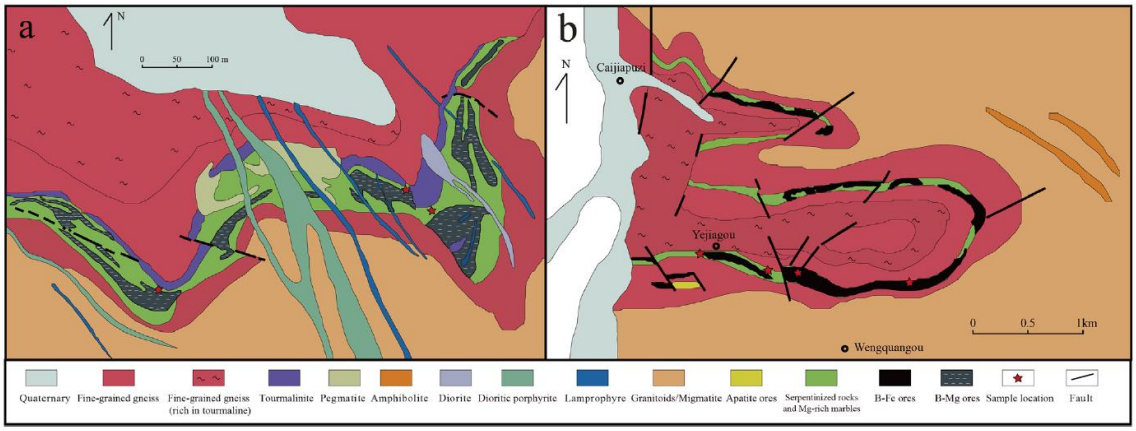
a
N
0 50 100 m
b
N
Caijiapuzi
Yejiagou
Wengquangou
0 0.5 1km
Quaternary
Fine-grained gneiss
Fine-grained gneiss (rich in tourmaline)
Tourmalinite
Pegmatite
Amphibolite
Diorite
Dioritic porphyrite
Lamprophyre
Granitoids/Migmatite
Apatite ores
Serpentinized rocks and Mg-rich marbles
B-Fe ores
B-Mg ores
Sample location
Fault

976 **Figure 3**

977

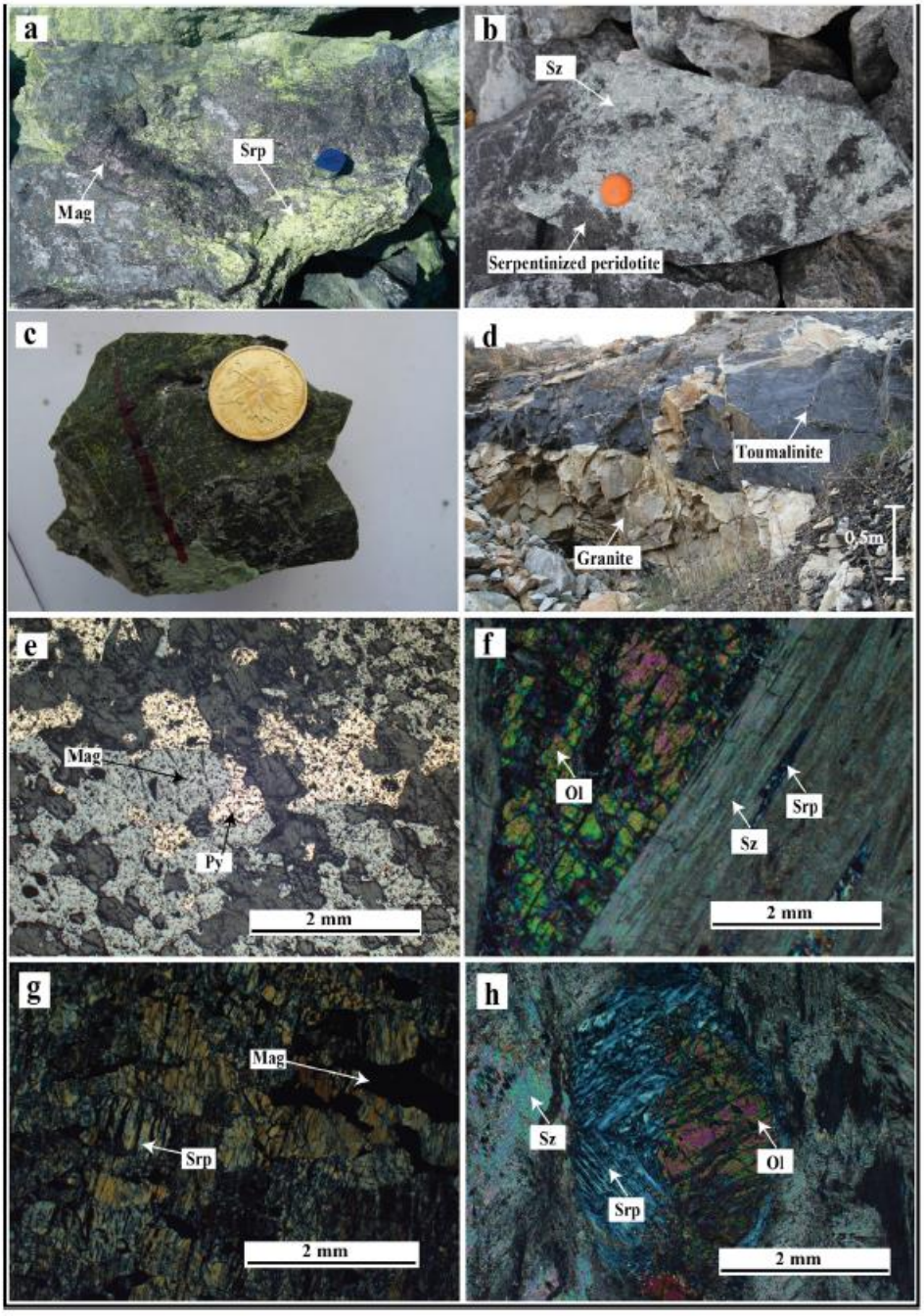

978

979

980

981

982 **Figure 4**

983

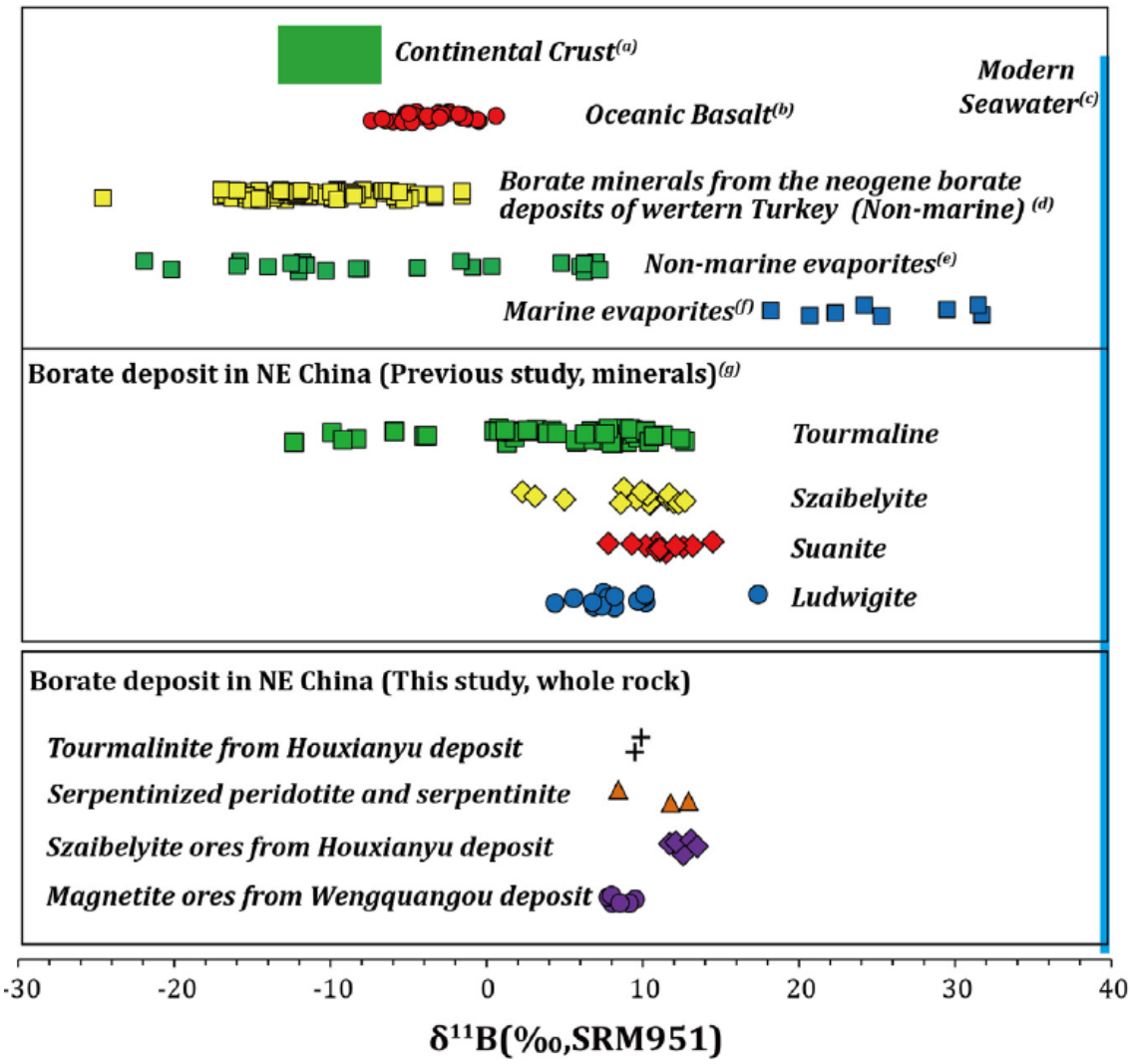

984

985

986

987

988

989

990

991 **Figure 5**

992

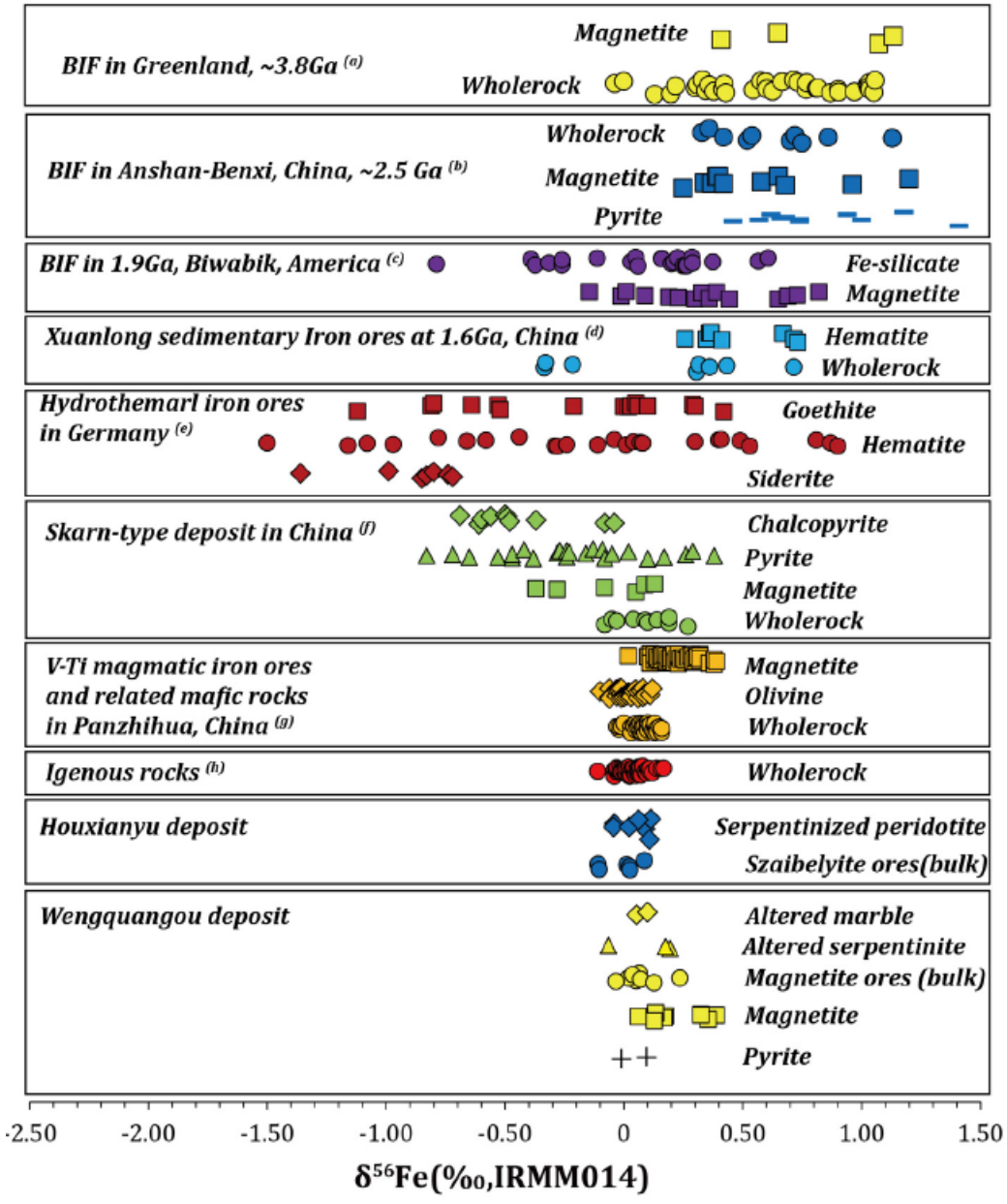

993

994

995

996

997

998 **Figure 6**

999

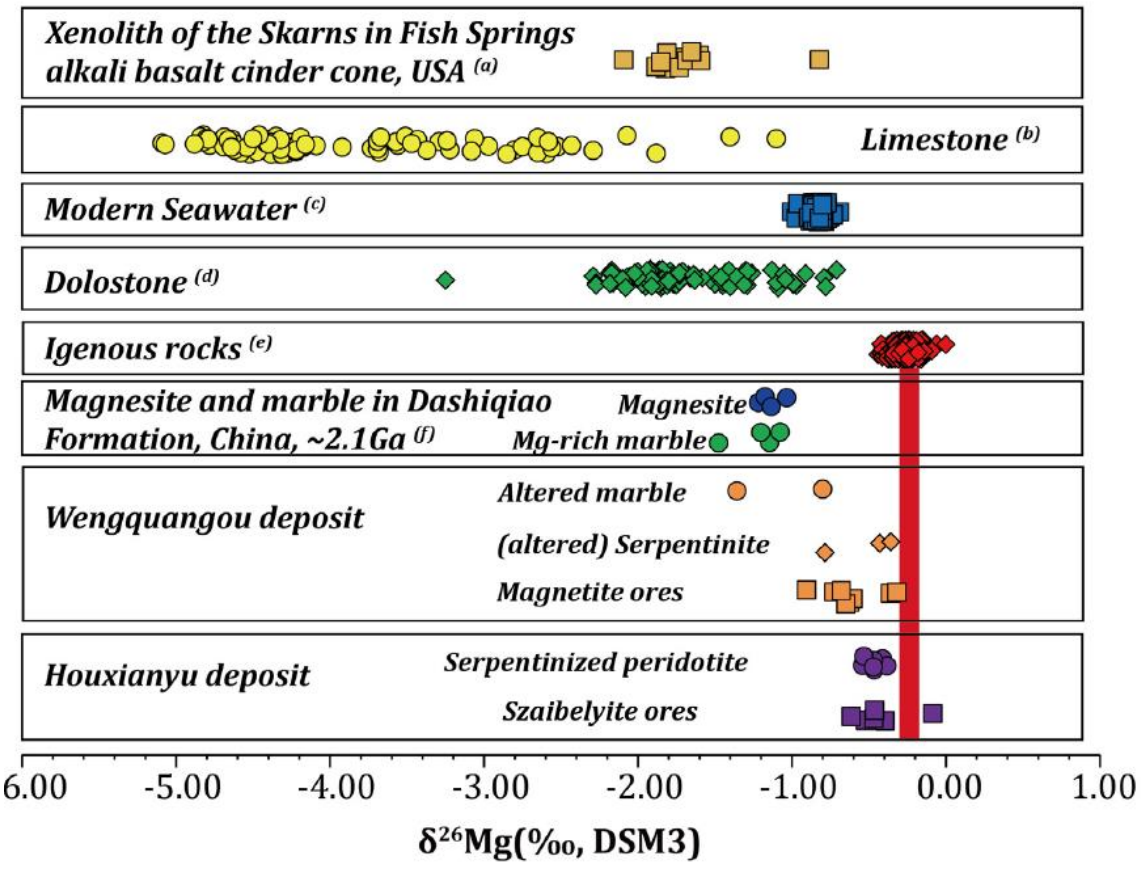

1000

1001

1002

1003

1004

1005

1006

1007

1008

1009

Figure 7

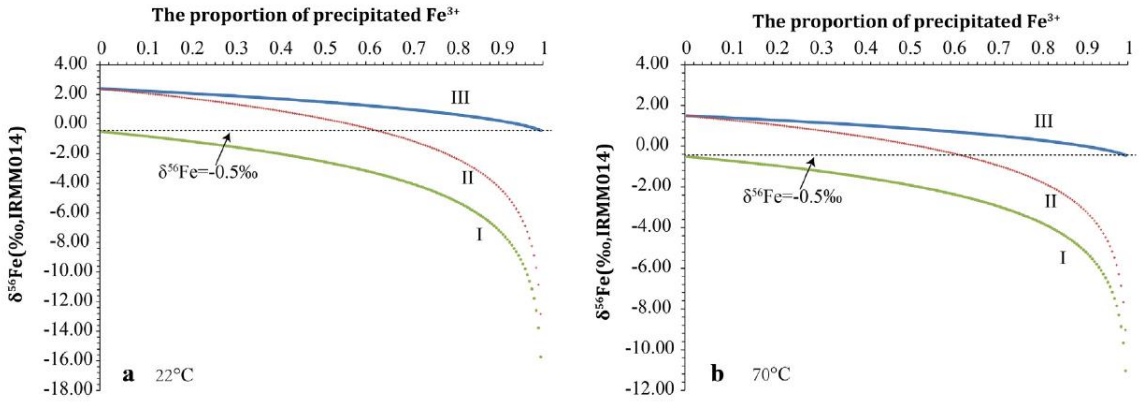
The proportion of precipitated Fe3+
δ56Fe(‰,IRM014)
δ56Fe=-0.5‰
III
II
I
a 22°C
b 70°C

Figure 8

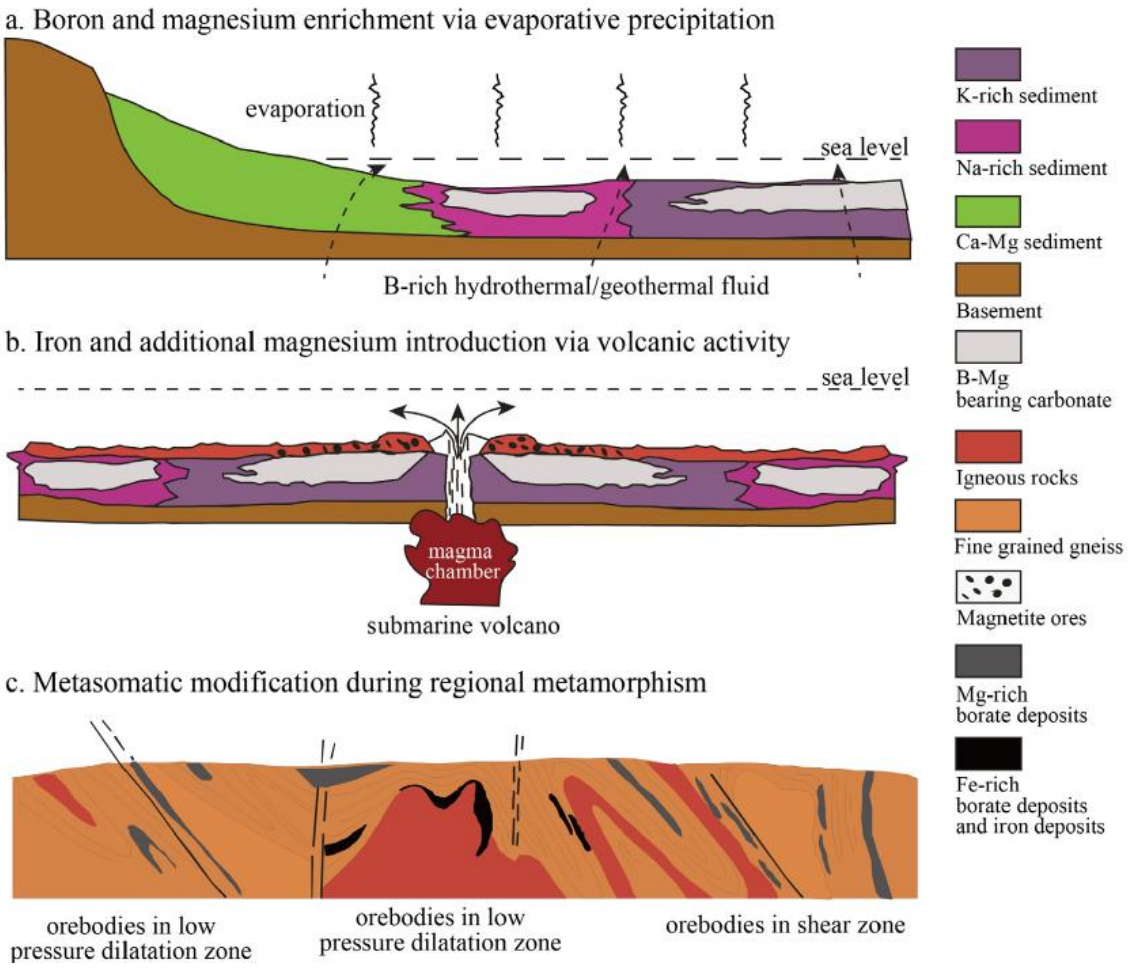
a. Boron and magnesium enrichment via evaporative precipitation
evaporation
sea level
B-rich hydrothermal/geothermal fluid
b. Iron and additional magnesium introduction via volcanic activity
sea level
magma chamber
submarine volcano
c. Metasomatic modification during regional metamorphism
orebodies in low pressure dilatation zone
orebodies in low pressure dilatation zone
orebodies in shear zone
K-rich sediment
Na-rich sediment
Ca-Mg sediment
Basement
B-Mg bearing carbonate
Igneous rocks
Fine grained gneiss
Magnetite ores
Mg-rich borate deposits
Fe-rich borate deposits and iron deposits

Table 1

Table 1
Boron, iron, and magnesium isotopic compositions of ores (associated minerals) and rocks from the Paleoproterozoic borate deposits in NE China (unit of ‰).

Sample	Type	Whole rock		Magnetite		Pyrite		Whole rock		Whole rock
		$\delta^{57}Fe$	$\delta^{56}Fe$	$\delta^{57}Fe$	$\delta^{56}Fe$	$\delta^{57}Fe$	$\delta^{56}Fe$	$\delta^{26}Mg$	$\delta^{25}Mg$	$\delta^{11}B$
HXY12-02A	Altered szaibelyite ores	0.00	0.01					−0.40	−0.21	12.7
	Repeat	0.02	0.02							
HXY12-04	Serpentinized peridotite	−0.03	−0.04					−0.48	−0.24	11.8
HXY12-04A	Serpentinized peridotite	−0.10	−0.04					−0.42	−0.20	
HXY12-05	Szaibelyite ores	−0.04	0.02					−0.53	−0.27	11.7
HXY12-06	Serpentinized peridotite	0.11	0.09					−0.39	−0.17	
HXY12-07	Serpentinized peridotite	0.16	0.11					−0.55	−0.26	
HXY12-12	Szaibelyite ores	0.16	0.08					−0.48	−0.21	12.6
HXY12-13	Serpentinized peridotite	0.03	0.02					−0.48	−0.22	
HXY12-14	Tourmalinite									9.5
HXY12-16	Szaibelyite ores	0.04	0.03					−0.47	−0.21	12.1
HXY12-17	Szaibelyite ores	−0.17	−0.11					−0.09	−0.02	13.1
HXY12-19	Tourmalinite									9.9
HXY12-20	Szaibelyite ores	−0.13	−0.10					−0.62	−0.30	13.5
HXY12-21	Serpentinized peridotite	0.20	0.11					−0.54	−0.26	
HXY12-26	Serpentinized peridotite	0.07	0.06					−0.48	−0.25	12.9
	Repeat							−0.46	−0.21	
WQG12-01	Magnetite ores	0.10	0.07	0.38	0.27			−0.63	−0.31	8.1
	Repeat							−0.66	−0.34	
WQG12-02	Magnetite ores	0.07	0.05					−0.37	−0.18	
WQG12-04	Magnetite ores	0.05	0.02					−0.74	−0.37	7.8
WQG12-05+	Altered marble	0.10	0.05					−1.37	−0.69	
WQG12-08	Magnetite ores	0.31	0.24	0.57	0.39			−0.61	−0.31	9.5
	Repeat	0.35	0.22							
WQG12-24	Altered serpentinite	−0.10	−0.06	0.13	0.06			−0.80	−0.40	8.4
	Repeat							−0.85	−0.42	
WQG12-25	Magnetite ores	0.06	0.04	0.47	0.32	−0.04	−0.01	−0.91	−0.45	8.0
WQG12-26	Altered serpentinite	0.28	0.20	0.24	0.18			−0.37	−0.16	
WQG12-28	Magnetite ores	0.12	0.07	0.26	0.17			−0.66	−0.34	9.2
WQG12-29	Magnetite ores	0.20	0.13	0.49	0.36			−0.69	−0.34	
	Repeat			0.41	0.25					
WQG12-31	Altered serpentinite	0.27	0.17	0.19	0.13			−0.44	−0.22	
	Repeat			0.09	0.06			−0.42	−0.21	
WQG12-33	Altered marble	0.16	0.10					−0.81	−0.43	
WQG12-34	Magnetite ores	−0.03	−0.03	0.19	0.13	0.10	0.07	−0.33	−0.14	8.5
	Repeat							−0.28	−0.13	

Appendix Table

Appendix Table
Major elements concentrations of ores (associated minerals) and rocks from the Paleoproterozoic borate deposits in NE China (unit of %).

Sample	Type	Description	SiO_2	TiO_2	Al_2O_3	TFe_2O_3	MnO	MgO	CaO	Na_2O	K_2O	P_2O_5	B_2O_3	LOI	Total
HXY12-02A	Altered szaibelyite ores	Altered by intense carbonatization and serpentinization, dominated by the mineral of magnesite, with moderate szajbelyite and less forsterite, lizardite, clinochlore	15.15	0.03	0.74	3.15	0.07	45.10	0.25	0.03	0.05	0.01	14.50	20.22	99.30
HXY12-04	Serpentinized peridotite	Altered by serpentinization and mineralization, dominated by the mineral of forsterite, with moderate lizardite and szajbelyite	32.20	<0.01	0.12	5.10	0.14	46.40	1.32	0.07	<0.01	0.17	2.71	11.93	100.16
HXY12-04A	Serpentinized peridotite	Altered by serpentinization, dominated by the mineral of forsterite, with less lizardite, dolomite, clinochlore and phlogopite	39.50	0.02	0.25	6.37	0.12	49.30	1.27	0.09	0.20	0.81	0.53	1.76	100.22
HXY12-05	Szaibelyite ores	Dominated by szajbelyite, with less lizardite, clinochlore and quartz	3.99	<0.01	0.06	3.69	0.10	45.00	0.36	0.02	<0.01	0.26	32.83	14.46	100.78
HXY12-06	Serpentinized peridotite	Altered by serpentinization, dominated by the mineral of lizardite, forsterite	36.50	<0.01	0.72	7.39	0.14	46.10	0.29	0.06	<0.01	0.01	0.56	8.35	100.12
HXY12-07	Serpentinized peridotite	Altered by serpentinization, dominated by the mineral of lizardite, forsterite	35.20	0.01	0.19	5.45	0.15	47.20	0.61	0.05	<0.01	0.04	0.50	10.39	99.78
HXY12-12	Szaibelyite ores	Dominated by forsterite and szajbelyite, with moderate magnesite	29.90	<0.01	0.14	6.75	0.10	47.00	0.79	0.04	0.01	0.15	7.02	7.38	99.28
HXY12-13	Serpentinized peridotite	Altered by serpentinization, dominated by the mineral of forsterite and lizardite	39.90	0.02	1.45	7.02	0.12	45.80	0.52	0.06	1.18	0.23	0.32	3.44	100.06
HXY12-14	Tourmalinite	Dominated by the mineral of tourmaline, with less quartz	36.30	0.98	26.30	9.04	0.02	9.61	1.85	2.06	0.05	0.23	10.15	2.85	99.44
HXY12-16	Szaibelyite ores	Dominated by szajbelyite and lizardite, with moderate magnesite	22.10	<0.01	0.45	3.01	0.09	41.80	0.56	0.02	<0.01	<0.01	12.89	18.59	99.51
HXY12-17	Szaibelyite ores	Dominated by szajbelyite, with moderate amphibole, phlogopite and less lizardite	21.50	0.04	1.36	2.98	0.07	36.10	4.05	0.13	1.18	0.18	23.62	7.95	99.16
HXY12-19	Tourmalinite	Dominated by the mineral of tourmaline, with less quartz	36.30	0.69	24.80	11.18	0.03	8.95	2.47	1.68	0.07	0.16	10.21	2.36	98.90
HXY12-20	Szaibelyite ores	Dominated by szajbelyite, with moderate magnesite and clinochlore	3.86	0.02	0.89	3.32	0.10	43.70	0.06	0.02	<0.01	<0.01	31.55	15.74	99.26
HXY12-21	Serpentinized peridotite	Altered by moderate serpentinization, dominated by the mineral of forsterite and lizardite	38.70	<0.01	0.13	8.03	0.12	48.20	0.33	0.08	0.04	0.19	0.31	4.48	100.61
HXY12-26	Serpentinized peridotite	Dominated by the mineral of forsterite, lizardite and szaibelyite	29.80	<0.01	0.16	7.23	0.11	47.10	0.12	0.04	0.12	0.08	9.70	5.36	99.82

(continued on next page)

Appendix Table (*continued*)

Sample	Type	Description	SiO_2	TiO_2	Al_2O_3	TFe_2O_3	MnO	MgO	CaO	Na_2O	K_2O	P_2O_5	B_2O_3	LOI	Total
WQG12-01	Magnetite ores	Dominated by the mineral of magnetite, with moderate lizardite, kaolinite and szaibelyite	8.74	0.05	1.42	63.80	0.07	16.90	0.12	0.09	0.48	0.09	4.53	2.49	98.78
WQG12-02	Magnetite ores	Dominated by the mineral of magnetite, lizardite and phlogopite	20.70	0.15	2.40	43.46	0.06	22.70	1.08	0.12	1.23	0.03	1.03	6.69	99.65
WQG12-04	Magnetite ores	Dominated by the mineral of szaibelyite, magnetite and lizardite, with less calcite, phlogopite	20.90	0.06	0.38	37.41	0.08	31.40	0.27	0.06	0.02	0.15	2.70	5.38	98.81
WQG12-05+	Altered marble	Altered by fluid metasomatism, dominated by the mineral of dolomite, with less lizardite and phlogopite	13.40	0.08	1.91	6.15	0.14	23.60	19.70	0.06	0.73	0.04	<0.06	33.56	99.37
WQG12-08	Magnetite ores	Dominated by the mineral of magnetite, with moderate humite and chlorite	9.91	0.08	0.74	66.72	0.07	18.50	0.03	0.06	<0.01	0.02	1.69	0.96	98.78
WQG12-24	Altered serpentinite	Aletered by minerelization, dominated by the mineral of lizardite, szaibelyite, with moderate magnetite	19.20	0.01	0.25	31.32	0.10	31.00	0.48	0.03	0.02	0.16	6.76	9.59	98.93
WQG12-25	Magnetite ores	Dominated by the mineral of magnetite and lizardite	15.05	0.04	0.66	50.51	0.06	25.60	0.10	0.06	0.10	0.08	2.05	4.05	98.36
WQG12-26	Altered serpentinite	Aletered by minerelization, dominated by the mineral of lizardite and magnetite	37.00	<0.01	0.03	9.95	0.02	37.00	1.80	0.04	0.01	1.24	0.79	12.20	100.08
WQG12-28	Magnetite ores	Dominated by the mineral of magnetite, lizardite, szaibelyite	14.80	0.09	1.48	39.49	0.05	27.60	0.14	0.09	0.63	0.08	7.20	7.18	98.83
WQG12-29	Magnetite ores	Dominated by the mineral of magnetite, lizardite, phlogopite, humite	16.90	0.10	0.56	50.28	0.06	26.10	0.08	0.06	0.10	0.07	1.09	3.25	98.64
WQG12-31	Serpentinite	Dominated by the mineral of lizardite, magnetite, with less calcite	35.60	<0.01	0.01	11.03	0.05	34.90	4.13	0.04	<0.01	0.14	0.34	14.36	100.60
WQG12-33	Altered marble	Altered by fluid metasomatism, dominated by the mineral of dolomite, with moderate magnesite and less quartz	16.95	0.02	0.21	21.85	0.06	15.75	11.30	0.02	0.01	<0.01	<0.06	32.50	98.67
WQG12-34	Magnetite ores	Dominated by the mineral of lizardite and magnetite, with less pyrrhotite and clinochlore	11.60	0.02	0.55	63.59	0.05	16.60	0.11	0.05	<0.01	0.06	1.06	5.56	99.26

1064